Full length article

Deformation faulting in a metastable CoCrNiW complex concentrated alloy: A case of negative intrinsic stacking fault energy?

Shaolou Wei, Cemal Cem Tasan*

Department of Materials Science and Engineering, Massachusetts Institute of Technology, Cambridge, MA 02139, USA

ABSTRACT

Microscopic crystalline defects are of fundamental importance in unraveling the plastic deformation response and thereby tailoring the macroscopic load-bearing performances of metallic alloys. Especially in the microstructural metastability engineering context of complex concentrated alloys (CCAs), while profuse interest has been focused on phase and twin boundaries as well as their interactions with glissile dislocations, stacking faults, as another essential planar defects, have remained comparatively less-explored and unutilized. In the present work, by investigating a metastable CoCrNiW CCA via the combination of *in-situ* synchrotron X-ray diffraction and *in-situ* electron channeling contrast imaging (ECCI), we show that stacking faults formation can also operate as the predominant deformation micro-mechanism, accommodating plastic strain while enabling macroscopic strain hardening. Through the examination of relative phase stability by thermodynamic modeling, we reveal that this sort of deformation faulting response is largely correlated with a negative intrinsic stacking fault energy. The corresponding physical revelation is explored in greater details regarding thermodynamics, structure, and mechanics, followed by *in-situ* experimental verification of the stacking fault activities.

© 2020 Acta Materialia Inc. Published by Elsevier Ltd. All rights reserved.

1. Introduction

Multi-principal-element alloys and the sub-branches of complex concentrated or high-entropy alloys (CCAs or HEAs) have triggered the pursuit of more exceptional mechanical and/or functional performances in the immense central portion of the multi-dimensional phase diagrams [1–5]. Structural alloys developed from this quick-emerging paradigm have already witnessed several salient advantages, such as outstanding strength-ductility synergy at cryogenic temperatures in the face-centered cubic (FCC) systems [6–8], and promising yield strength preservation at elevated temperatures in the refractory body-centered cubic (BCC) systems [9–11]. Especially in FCC-structured CCAs, provided their desirable ductility and damage tolerance, the comparatively deficient strength and strain hardenability have given rise to dedicated effort in exploring possible strengthening mechanisms [12–15]. While the prototypical CCAs design strategy specifically seeks to stablize a random single-phase solid solution microstructure via configurational entropy maximization [2,16], their intrinsic metastable nature in the thermodynamic front [17–20] inspires the advancement of mechanically metastable CCAs [21]. The latter, on

the other hand, has in turn driven an intense momentum in elucidating the plastic deformation micro-events [22–25].

Similar to conventional dilute FCC-alloys, crystalline defects and their stability are of fundamental importance in the deformation response of metastable CCAs [26–28]. Critically, intrinsic stacking fault energy (γ_{iSFE}), has been recognized as an effective indicator in implying the mechanical stability, since it signifies the propensity for a $a/2\langle110\rangle$ perfect dislocation to dissociate into paired $a/6\langle112\rangle$ glissile partials [29]. Exemplary investigations of the metastable quaternary FeMnCoCr system [21] and its ramifications [30] have showcased the tunability of operating deformation modules via different γ_{iSFE}, including perfect dislocation glide, mechanical twinning, and strain-induced FCC-hexagonal close packing (HCP) martensitic transformation. As such, numerous experimental effort has then been devoted into the understanding of compositional dependency for the competing deformation modules [31,32], and more recent literature also demonstrates the intriguing role of local chemical inhomogeneity in affecting the partial and/or perfect dislocation pathways within these heavily alloyed systems [33–35]. In light of the defects category that can be potentially involved, although extensive focus has been directed to glissile dislocations, FCC/HCP phase boundaries, and $\Sigma3$ coherent twin boundaries, the other important planar defects, stacking faults, have not yet drawn sufficient attention [36,37]. Current understanding of stacking faults' role in plastic deformation

of metastable CCAs largely remains at the extent that they are structural embryos for HCP-martensite nucleation, which is an apparent inference from the Olson-Cohen martensitic transformation theory [38,39]. In an atomistic standpoint, however, mechanically nucleating a mono-layered intrinsic stacking fault involves a $|a/6\langle112\rangle|$ shear on the corresponding {111} glide plane, being a micro-mechanism that also enables plastic strain accommodation. If the foregoing partial gliding event manages to occur on every other {111} plane, then the FCC-HCP martensitic transformation will consequently take place [40]. One fundamental proposition remains unclear considering this sort of atomistic analogy is that: can stacking fault formation by itself become the major plasticity carrier once they are sufficiently stable?

Amongst the very few systems (He, Fe, Co, Tl, Pb, and Yb) that can undergo direct FCC-HCP transformation throughout the periodic table [41,42], Fe- and Co-based alloys have created profound interest in exploring improved mechanical performances and the underlying deformation micro-events [43–45]. The most conspicuous feature that distinguishes Co-rich system from others lies in its absence of body-centered cubic (BCC) structure in the corresponding phase diagram [42,46]. Earlier diffuse neutron scattering investigation of pure Co and Co-Ni dilute alloys evidenced the long-ranged coherent modulated structures during FCC-HCP transformation, which signifies the mild interfacial lattice mismatch [41]. This sort of characteristics imply that the nucleation of substantial planar defects in Co-rich system could become predominant, once appropriate thermodynamic and mechanical boundary conditions are imposed. In fact, more recent report of CCAs or HEAs with Co-rich compositions underpins the reduced activity of perfect glissile dislocations [47–49], and the corresponding *ab-initio* simulation [32,49,50] also indicates the comparatively low or even negative γ_{iSFE}. These intriguing features render Co-rich metastable CCAs as optimal candidates to systematically examine the foregoing proposition towards stacking faults.

Quantitative assessments of stacking fault evolution during plastic deformation indispensably rely on real-time characterization techniques that possess an optimal balance between view-of-field and spatial resolution. While transmission electron microscope (TEM) reveals broad applications in probing dislocation morphology, stacking faults, and nano-twins in various CCAs [23,24,51], its narrow view-of-field appears rather deficient in providing statistically representative correlation between deformation micro-events and the macroscopic mechanical response. Synchrotron-X-ray diffraction, on the other hand, enables *in-situ* quantitative excerption of microstructure-level information of bulk alloys [52–54], including phase constitution change [25,55], lattice strain evolution [56,57], and stacking fault fraction variation [25]. However, its shortcomings mostly exist in the insufficiency in realizing direct correlation to the microstructural features in real space. A quick-emerging scanning electron microscope (SEM)-based technique, electron channeling contrast imaging (ECCI) [58,59], does manage to complement some of these limitations. With a comparatively wider view-of-field and a satisfactory spatial resolution (down to 50-80 nm) as well as the capability in excerpting crystallographic information once coupled with electron backscatter diffractometry (EBSD), ECCI has received increasing attention in revealing the defect substructural evolution associated with plastic deformation and/or phase transformations in a broad spectrum of metallic alloys [60–64].

In the present work, by investigating a metastable $Co_{60}Cr_{25}Ni_{10}W_5$ CCA through coupled *in-situ* synchrotron X-ray and *in-situ* ECCI approaches, we validate that a significant amount of stacking faults is generated in response to external loading, contributing to the macroscopic strain hardening. Through theoretically examining the phase stability of the present alloy, we propose that this kind of less-explored "deformation faulting"

micro-event is correlated with a negative γ_{iSFE}, for which the corresponding physical revelation and validity are re-visited from thermodynamic, structural, and mechanical perspectives. Direct experimental evaluation of stacking fault activity during elastic loading-unloading cycle is showcased to verify the theoretical postulates. Through systematic exploration of the deformation sub-structures, we assert that sessile dislocation nucleation resulting from the intersection between unparallel stacking faults and elastic repulsion between parallel stacking faults are the two major micro-mechanisms that provide strain hardenability. Broader insights into mechanistically-driven metastable CCAs/HEAs design strategy are also discussed.

2. Material and methods

2.1. Ex-situ mechanical testing and microstructural characterizations

The quaternary CCA exploited for the present study exhibits a nominal composition of $Co_{60}Cr_{25}Ni_{10}W_5$ at.%, provided by Allegheny Technologies Incorporated (ATI), Natrona Heights, PA, USA. Meso-scale microstructural characterizations including morphological investigations, ECCI, energy-dispersive X-ray spectroscopy analyses (EDS, EDAX Octane Elite Plus detector), and EBSD (EDAX Hikari camera) were accomplished in a TESCAN MIRA 3 SEM. All the EBSD patterns were post-analyzed in an Orientation Imaging Microscopy (OIM) software for quantitative assessments of microstructural characteristics. As presented in Fig. 1 (a) and (b), the CoCrNiW CCA demonstrates an equiaxed grain morphology with an average grain size of ~34 μm (excluding annealing boundaries, details see supplementary Fig. S1) with a single FCC phase constitution at the undeformed state (lattice constant a=3.58929 Å, measured by synchrotron X-ray, details see section 2.2). Further EDS elemental mapping taken across multiple grain boundaries confirms that all the four principal alloying elements exhibit spatially uniform distributions (Fig. 1 (c1)-(c4)). As such, the influence of compositional inhomogeneity on the deformation modules can be excluded at the meso-scale. Rectangular dog bone-shaped specimens with a gauge geometry of 6.5 × 2.5 × 1.0 mm^3 were section by electrical discharge machining (EDM) from bulk alloy sheet for uniaxial tensile testing at an ambient temperature (298 K). These specimens were subjected to mechanical grinding on a series of SiC abrasive papers before speckle patterns were coated onto their surfaces for optical digital image correlation (DIC) study. Uniaxial tensile experiments were performed on a Deben Gatan micro-mechanical testing platform with a strain rate of 1 × 10^{-3} s^{-1}. To examine the local strain evolution characteristics, digital images were acquired every 500 ms during tensile tests and analyzed via a GOM open-access software (https://www.gom.com/3d-software/gom-correlate.html).

2.2. In-situ deformation under synchrotron X-ray radiation

In-situ synchrotron X-ray experiments were performed at beamline ID 11-C, Argonne National Laboratory, Chicago, USA. Fig. 2 schematically illustrates the experimentation for *in-situ* tensile testing (a picture for the actual configuration is provided in supplementary Fig. S2): dog bone-shaped specimen with a gauge geometry of 8.0 × 2.0 × 1.5 mm^3 was subjected to quasi-static tensile loading (strain rate: 1 × 10^{-3} s^{-1}) under high-energy synchrotron X-ray radiation (wavelength: 0.1173 Å). DIC technique with an acquisition frame rate of 0.2 Hz was employed to ensure a precise strain measurement and thereby the calculation of strain hardening rate as well as strain hardening exponent. During the deformation procedure, two-dimensional diffractograms were recorded every 1.0% engineering strain incrementation until fracture. To unambiguously characterize the lattice strain evolution [65–67], the two-
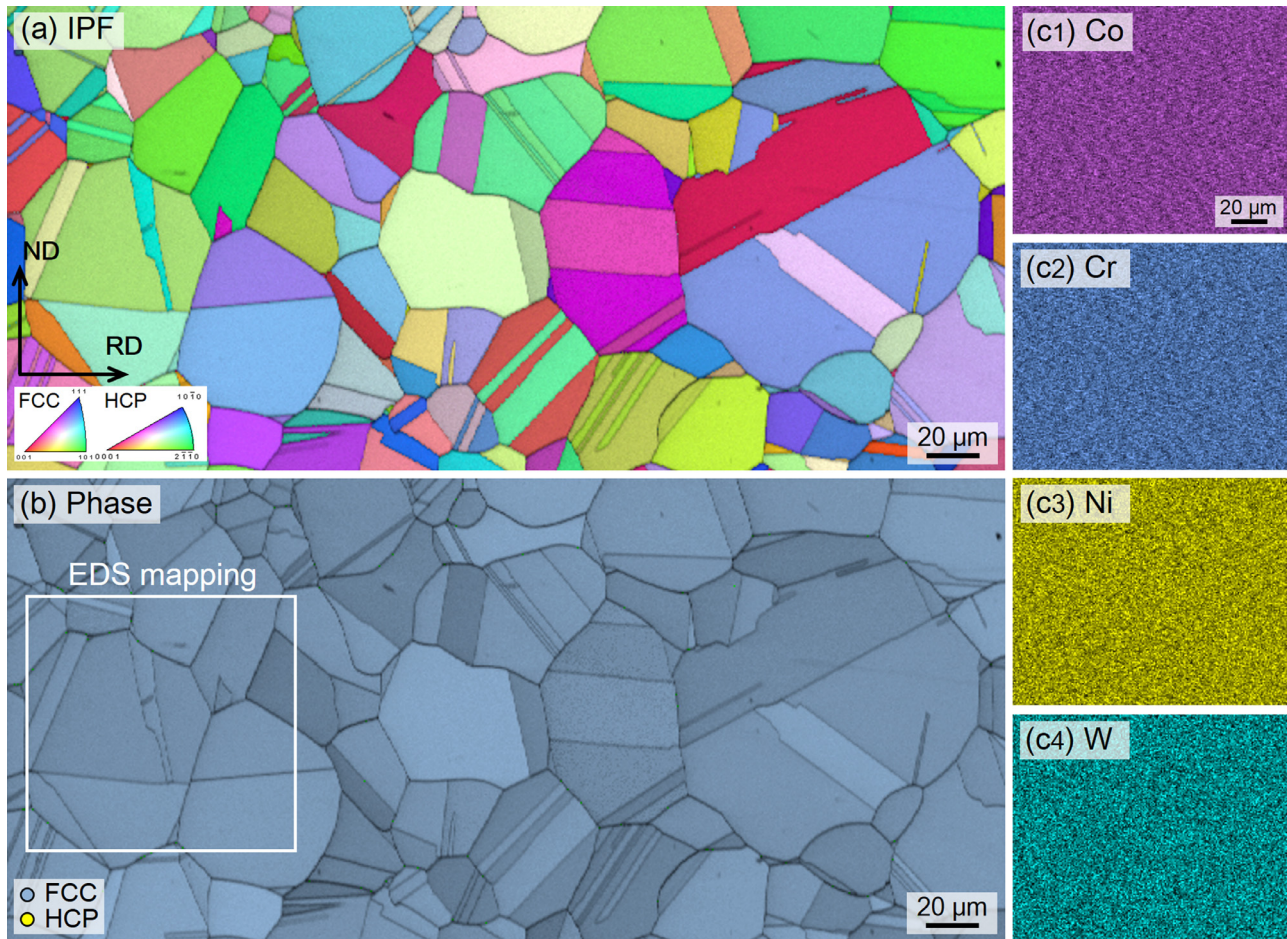
Fig. 1. Microstructural characterization of the $Co_{60}Cr_{25}Ni_{10}W_5$ CCA at the undeformed state: (a) EBSD inverse pole figure (IPF) showing the equiaxed grain morphology; (b) phase map confirming the single FCC-phase constitution; (c1)-(c4) EDS elemental mapping for Co, Cr, Ni, and W in the selected region of interest denoted in (b), here the same scale bar is applied. Detailed grain size distribution chart is provided in supplementary Fig. S1.
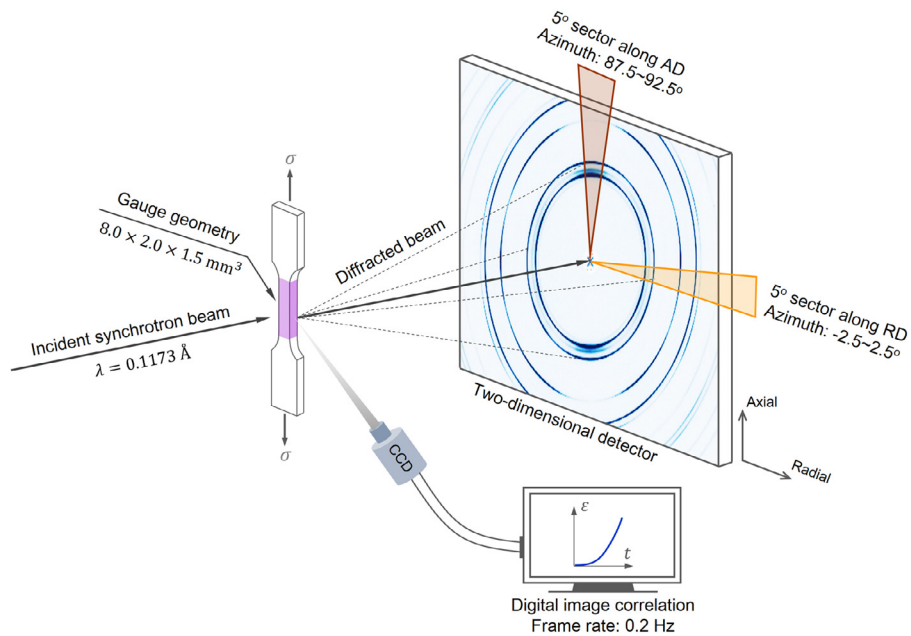

Fig. 2. Schematic for the *in-situ* synchrotron X-ray diffraction experimentation and the acquisition for axial and radial diffraction patterns. An actual image of the setup is provided in supplementary Fig. S2.
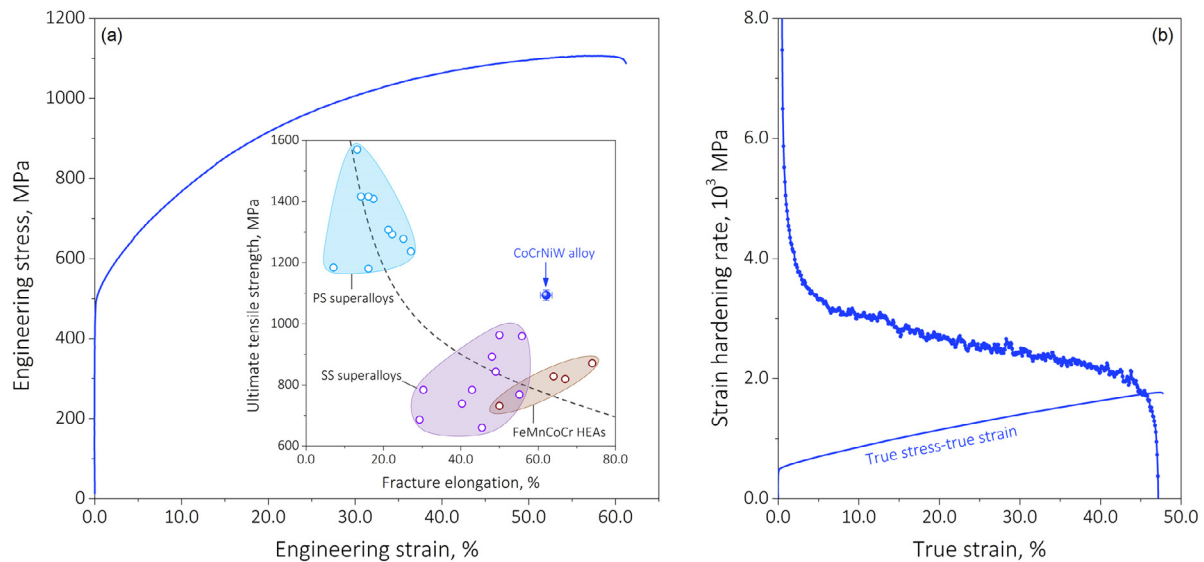
Fig. 3. Room-temperature mechanical response under uniaxial tensile loading: (a) engineering stress-strain curve; (b) strain hardening rate chart. The inset of (a) demonstrates an Ashby comparison amongst the present $Co_{60}Cr_{25}Ni_{10}W_5$ CCA and commercial superalloys [69] as well as the latest metastable FeMnCoCr HEAs [62,70]. Abbreviations adopted: precipitation-strengthened (PS); solid-solution strengthened (SS).

dimensional diffractograms were sectioned into 5 deg. sectors respectively along axial (parallel to the loading axis) and radial (perpendicular to the loading axis) directions before being integrated as a function of the corresponding azimuth angles. The integrated patterns were subsequently Rietveld-fitted using GSAS-II [68] and Matlab software for determining quantitative parameters for further mechanistic explorations.

3. Results

3.1. Uniaxial tensile response and deformation substructure characterizations

Fig. 3 reveals the uniaxial tensile property of the $Co_{60}Cr_{25}Ni_{10}W_5$ CCA: it yields at ~498 MPa, followed by a pronounced strain hardening process (Fig. 3 (b)), reaching an ultimate tensile strength of ~1100 MPa and a fracture elongation of ~61.2%. Compared with the commercial solid-solution or precipitation strengthened superalloys [69] with similar chemical constitutions, as well as the latest metastable FeMnCoCr HEAs [62,70] where extensive mechanically-induced martensitic transformation takes place, a more improved strength-ductility is indeed achieved in the present CCA. Such intriguing mechanical properties render careful explorations of the underlying deformation micro-events, which will be detailed next, starting with post-mortem ECCI/EBSD analyses.

Unlike the typical electron channeling contrast produced by the surface networks of perfect dislocations in FCC crystals, ECCI micrographs here clearly reveal the presence of mono-layered planar-like features already at the low local strain levels (Fig. 4 (a) and (b)). Here, a brief discussion of the imaging technique is required to clarify the underlying assumptions and uncertainties. It should be noted that while the ECCI technique demonstrates salient advantages in resolving crystalline defects with a broad view-of-field, inaccuracies or artifacts may potentially arise from its deficiency in enabling quantitative diffraction analysis of specific local sites [59]. To unambiguously distinguish the defect category, we present in supplementary Fig. S3 the quantitative contrast profile assessments together with systematic comparisons to other representative deformation substructures, including perfect dislocations (both

wavy and planar morphologies) and mechanically-induced martensite. Two distinctive features are subsequently recognized for the present planar-like structures, evidencing the fact that they are stacking faults: (1) compared with perfect dislocations, the channeling contrast they produce exists in a much wider planar regime; and (2) the channeling contrast seen in Fig. 4 exhibits asymmetric characteristics (also see supplementary Fig. S3 (a) and (b)), namely, a straight bright edge on one side with a smoothly fading contrast on the other, differing from the symmetric contrast produced by thin twins or martensitic plates [59]. With elevating local strain level, these stacking faults not only reveal an increasing trend in their densities but also the activation of different faulting systems (Fig. 4 (c) and (d)). The latter, is confirmed from the intersections of unparallel faulting plane traces (Fig. 4 (c)). These results validate that in contrast to the negligible role of perfect dislocation glide, stacking faults prevail in the present alloy at the examined deformation levels, which consolidates the quantification of their evolutionary features based on synchrotron X-ray diffraction technique (see Section 3.2).

By coupling EBSD and ECCI analyses in the region with an even higher local strain level of ~25.2%, it is shown that at the length-scale of grain-size (Fig. 5 (a1)), no clear trait of characteristic misorientation change that corresponds to mechanical twins or blocky HCP-martensite is observed from the inverse pole figure (IPF, Fig. 5 (b1)) or phase map (Fig. 5 (c1)). ECCI micrograph taken at a higher magnification again verifies that stacking faults belong to the $(1\bar{1}1)$ plane are densely populating in the grain interior, which diminishes the channeling condition (Fig. 5 (a2)). The corresponding EBSD results (Fig. 5 (b2) and (c2)) also suggest the absence of twins (see supplementary Fig. S4 for more detailed analysis) or martensite in this region at the spatial resolution limit of ~30 nm. The foregoing deformation substructures, if compared with perfect dislocation-mediated plasticity in conventional FCC-metals or mechanically metastable ones that exhibit twinning or martensitic transformation at a similar deformation level, can be concluded that it is the formation of an extensive amount of stacking faults that acts as the predominant mechanism accommodating macroscopic plastic strain. As such, in the following discussion, we exploit the term "deformation faulting" to comply with the mechanistic origin of this micro-event and the literature [71–73].
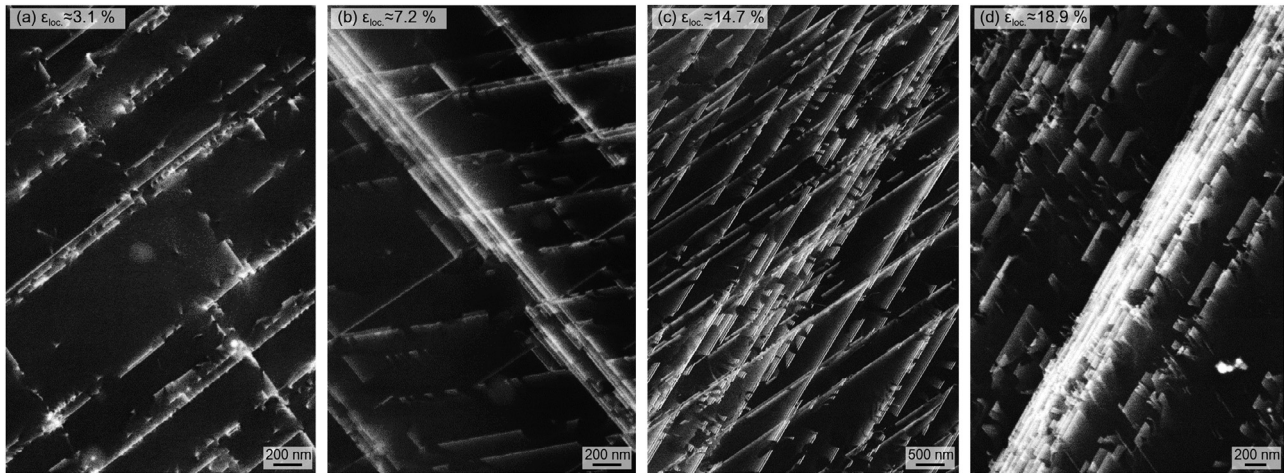
Fig. 4. ECCI characterization of deformation substructures: (a)-(d) stacking faults' structure evolution with respect to increasing local strain level. A systematic comparison in light of the channeling contrast produced by perfect dislocations, stacking faults, and thin HCP-plate is provided in supplementary Fig. S3.
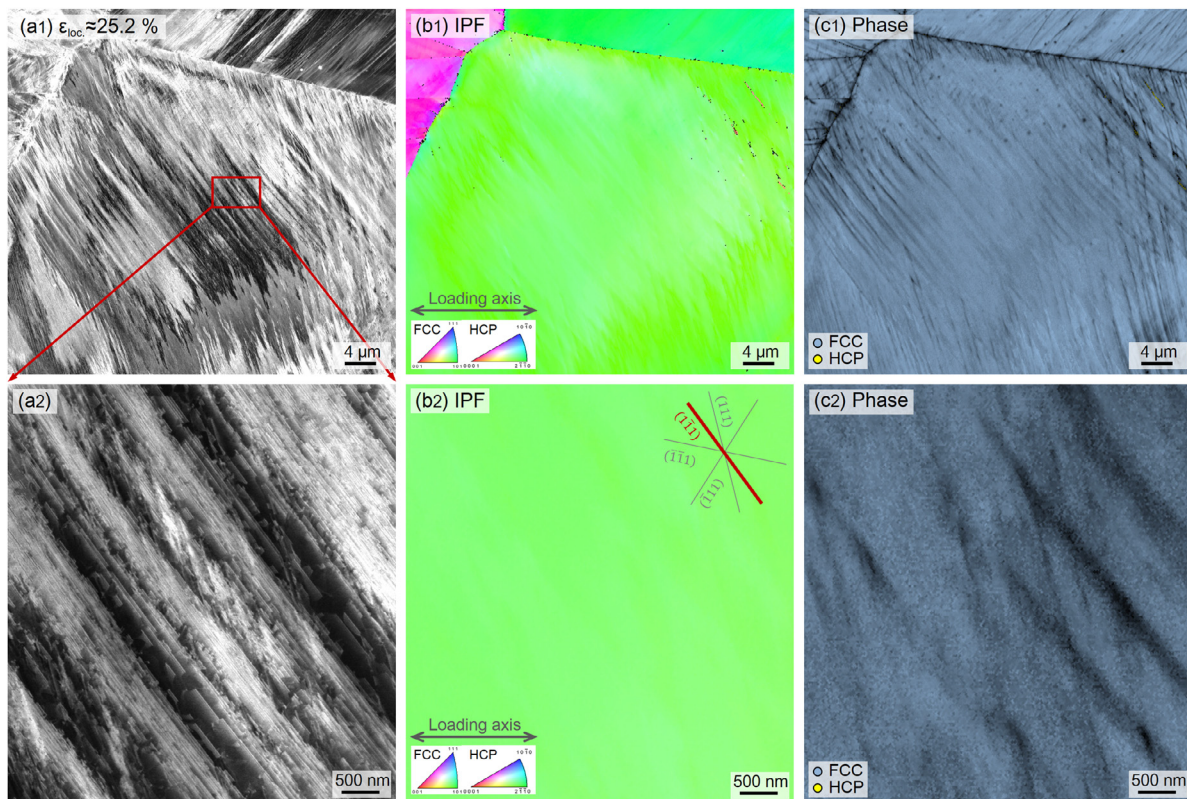

Fig. 5. Coupled EBSD and ECCI analyses for stacking faults at a comparatively high local strain level of ~25.2%: (a1) and (a2) lower and higher magnification ECCI micrographs; (b1) and (b2) EBSD IPF maps eliminating the formation of nano-twins; (c1) and (c2) EBSD phase maps confirming the FCC structure in the observed region. More detailed misorientation line profile analysis for eliminating mechanical twin formation is presented in supplementary Fig. S4.

3.2. In-situ deformation investigation via synchrotron X-ray diffraction

To assess the evolutionary characteristic of stacking faults and thereby to also quantify their roles in plastic deformation, the $Co_{60}Cr_{25}Ni_{10}W_5$ CCA was subjected to *in-situ* synchrotron X-ray analyses. Fig. 6 provides the integrated diffraction patterns along axial (parallel to the loading axis) and radial (vertical to the loading axis) directions with respect to elevating deformation level until macroscopic fracture, general features of which are briefly summarized in three respects, followed by more detailed discussions: (1) while FCC-phase is maintained as the major phase constituent, additional peaks correspond to HCP-structure start to appear at relatively higher strain levels (~25.0% engineering strain); (2) owing to the Poisson's contraction effect, diffraction peaks at the axial direction (Fig. 6 (a)) shift to lower 2θ region (higher d-spacing) while the corresponding radial diffraction peaks (Fig. 6 (b)) witness an opposite shifting trend; and (3) as plastic straining proceeds, the diffraction peaks exhibit distinctive variation in their intensities. Intriguingly, the intensity of the $(220)_{FCC}$ peak decays and eventually vanishes at the later stage of deformation.

The variation in phase constitution during plastic deformation suggests that the present $Co_{60}Cr_{25}Ni_{10}W_5$ CCA exhibits somewhat mechanical metastability. To unambiguously quantify the phase
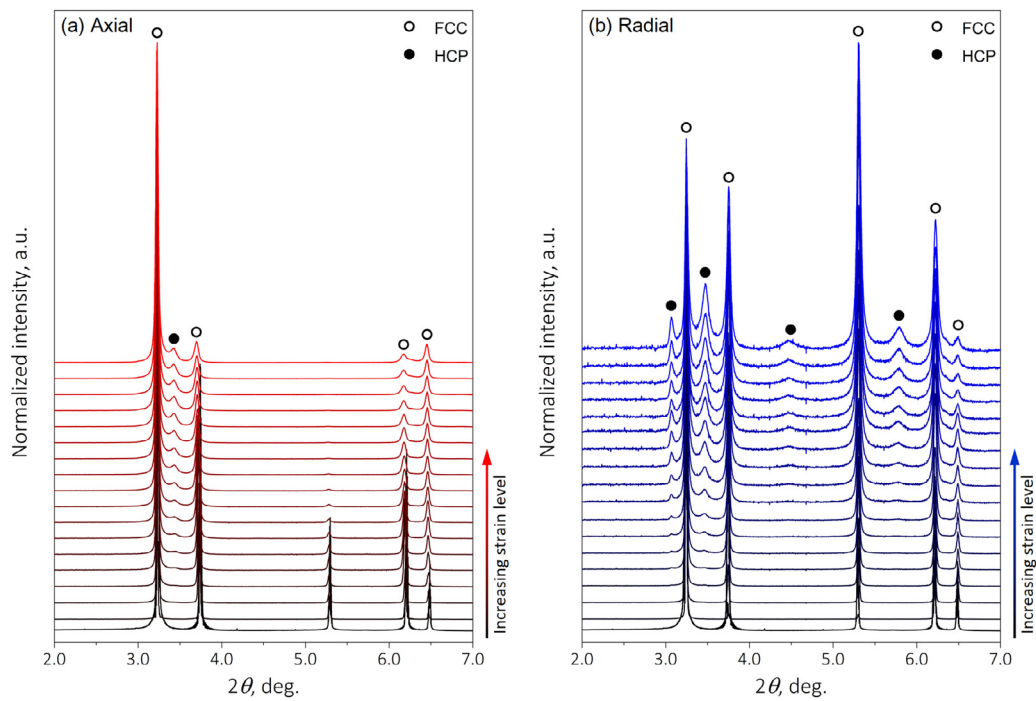
Fig. 6. One-dimensional diffraction patterns integrated along (a) axial and (b) radial directions. The selected sectors are schematically shown in Fig. 2.
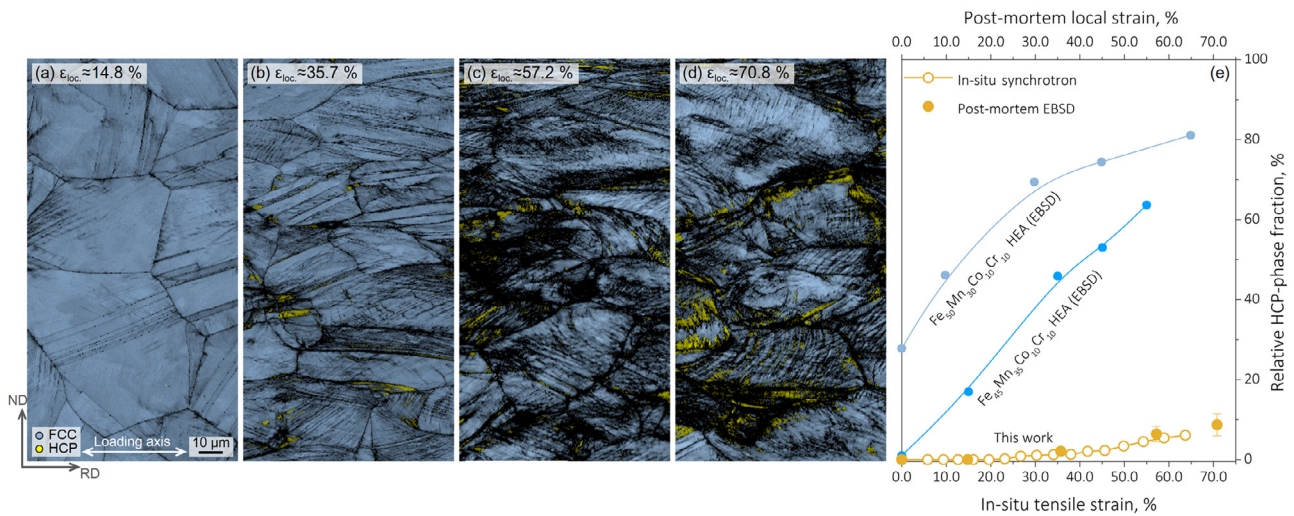

Fig. 7. Examination of phase stability during plastic deformation: (a)-(d) post-mortem EBSD phase maps acquired at increasing local strain levels (the same scale bar is applied); (e) phase fraction variation as a function of deformation level. Here, to enable a precise confirmation of the minor role of HCP-phase formation in the present CCA, phase fractions respectively determined from the *in-situ* synchrotron diffractograms (using full azimuth angle integration) and the foregoing EBSD analyses are plotted in the same chart. Representative data for FeMnCoCr HEAs are excerpted from the literature [62,70]. More detailed confirmation of the absence of mechanical twins is presented in supplementary Fig. S5.

fraction evolution and to also complement the foregoing characterization by ECCI (Figs. 4 and 5), we have evaluated the contents of these two present phases by both post-mortem EBSD analysis and Rietveld refinement of the two-dimensional *in-situ* diffractograms. As seen in Fig. 7, the HCP-phase does not witness any discernable increase in its fraction before the deformation level exceeds ~40.0% strain. The *in-situ* synchrotron X-ray diffraction results (Fig. 7 (e)) confirm that the total HCP-phase fraction only reaches ~6.0% at ~65.0% strain which is approximately the elongation-to-fracture (see the stress-strain curve in Fig. 3 (a)). It is also recognized from the EBSD phase maps that the HCP-phase mostly nucleates at grain boundaries (Fig. 7 (b) and (c)), without eminently growing into blocky morphologies even at a compara-

tively high local strain level of ~70.8%. In comparison with typical quaternary FeMnCoCr-type HEAs [62,70] where the strain-induced FCC-to-HCP martensitic transformation is dominant in the whole plastic realm, the evidently low HCP-phase fraction with minute dimension, the highly sluggish formation rate, and the fact that it only operates at the later deformation stage, all lead to the conclusion that the prototypical mechanically-induced phase transformation is largely impeded and playing a minor role in the present $Co_{60}Cr_{25}Ni_{10}W_5$ CCA. In addition, EBSD analyses also verify the absence of mechanical twin nucleation at the foregoing local strain levels, for which more detailed assessments are presented in supplementary Fig. S5. As such, by combining the foregoing EBSD/ECCI characterizations (Figs. 4 and 5) and the *in-situ* synchrotron X-ray
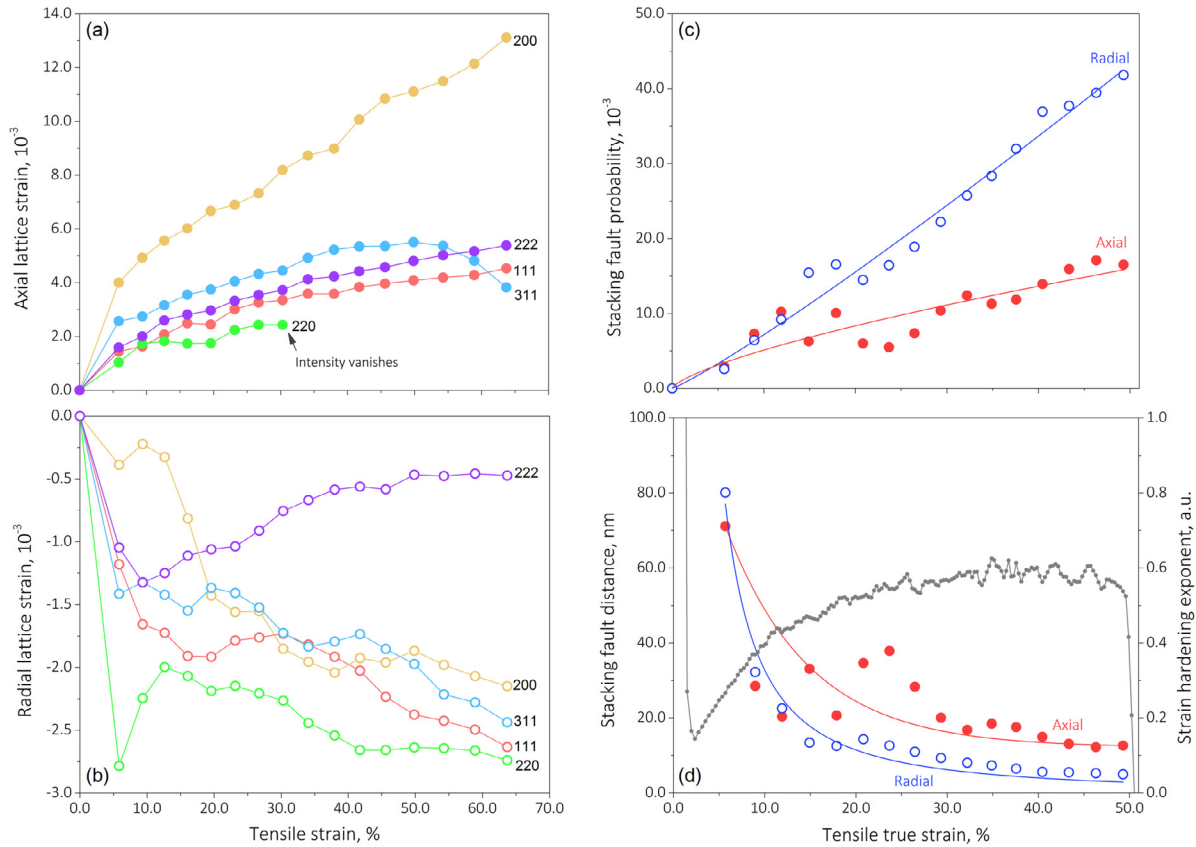
Fig. 8. Quantitative analyses of the *in-situ* synchrotron X-ray diffractograms: (a) and (b) axial and radial lattice strain evolution as a function of increasing deformation level; (c) radial and axial stacking fault probability versus tensile true strain; (d) correlation between stacking fault distance reduction and strain hardening rate elevation.

measurement, it is therefore conclusive that deformation faulting indeed acts as the major micro-mechanism in accommodating external plastic strain. Atomistic correlation between faulting and the FCC-to-HCP martensitic transformation as well as the insights into metastable alloy design will be discussed in Section 4.2.2.

The peak shift due to external plastic loading is next exploited to calculate apparent lattice strain via:

$$\varepsilon_{hkl}^{app.} = \frac{d_{hkl} - d_{hkl}^{o}}{d_{hkl}^{o}} \tag{1}$$

where d_{hkl} and d_{hkl}^{o} respectively denote the *d*-spacing of plane *hkl* at a certain deformation level and the undeformed state. In the axial direction (Fig. 8 (a)), except for 311 plane, lattice strains in all other planes reveal a monotonic increasing trend as a function of elevating global tensile strain. Amongst them, 200 plane exhibits the most pronounced resistance to plastic deformation, which is characterized by the highest lattice strain throughout the experimental realm, being consistent with the typical behavior of FCC-metals [74,75]. 220 plane, in contrast, witnesses the lowest lattice strain, suggesting the strongest propensity for plastic incipience. The corresponding intensity, on the other hand, also ceases to vanish as the global strain reaches ~30.0%, which is largely ascribed to the deformation texture developed during plastic straining [73,74,76]. To uncover the mechanism for the anomaly drop of the lattice strain in the 311 plane (Fig. 8 (a)), we have assessed its sub-reflection units by de-convoluting the experimentally measured diffraction pattern at a representative higher strain level. The analysis presented in supplementary Fig. S6 confirms that it is the formation of extensive amounts of extrinsic stacking faults that leads to pronounced asymmetric peak shifting and broadening in $h + k + l = \pm 5$ and $h + k + l = \pm 1$ sub-reflection units [77].

This sort of variation in diffraction characteristics shifts the apparent 311 peak towards higher 2θ region (i.e. smaller d_{311}), which in turn brings about the decrease in $\varepsilon_{311}^{app.}$, according to Eq. (1).

The presence of stacking faults also gives rise to the asymmetric evolution of lattice strains in 111 and 222 planes for both axial and radial directions, namely, the noticeable difference in the corresponding lattice strains provided their identical crystallographic symmetry. Note that while the Poisson's contraction effect renders negative lattice strain along the radial direction (Fig. 8 (b)), the distinction between $\varepsilon_{111}^{app.}$ and $\varepsilon_{222}^{app.}$ is still unambiguously resolved. In fact, according to diffraction theory [78,79], the lattice strain $\varepsilon_{hkl}^{app.}$ determined from apparent peak shift is comprised of two components:

$$\varepsilon_{hkl}^{app.} = \varepsilon_{hkl}^{sym.} - \frac{\sqrt{3}}{4\pi} \frac{\sum_{b} h + k + l}{(u+b)(h^2 + k^2 + l^2)} P_{sf} \tag{2}$$

in which, $\varepsilon_{hkl}^{sym.}$ originates from macroscopic straining and exhibits an elastic characteristic (regardless of crystalline defects), whereas, the inelastic portion $-\frac{\sqrt{3}}{4\pi} \frac{\sum_{b} h+k+l}{(u+b)(h^2+k^2+l^2)} P_{sf}$ is owing to the presence of stacking faults. Here u and b represent the number of unbroadened and broadened sub-reflection units in plane *hkl*, and P_{sf}, the stacking fault probability, is a direct measurement of the fraction for uncorrelated stacking faults within the tested specimen. Since $\varepsilon_{111}^{sym.}$ and $\varepsilon_{222}^{sym.}$ are identical in 111 and 222 planes, the corresponding P_{sf} can be expressed as an explicit function of the apparent lattice strains:

$$P_{sf} = \frac{32\pi}{3\sqrt{3}} \left(\varepsilon_{222}^{app.} - \varepsilon_{111}^{app.} \right) \tag{3}$$

As presented in Fig. 8 (c), the calculated P_{sf} of both axial and radial directions demonstrates a significant increase with respect

to elevating deformation level, respectively reaching 15.8×10^{-3} and 42.3×10^{-3} before macroscopic failure takes place. These P_{sf} quantities are particularly higher than those determined from FCC-structured alloys where perfect dislocation glide [73] operates as the major plastic deformation module, suggesting the comparatively salient role of extensive stacking fault formation (also see Figs. 4 and 5 as reference). It should be pointed out that since synchrotron X-ray appears rather deficient in unambiguously distinguishing the contribution of perfect and partial dislocations, the *a priori* condition of solely applying Eq. (3) in the analyses lies in the validation of negligible activity of perfect dislocations via complementary experiments. A rationally reliable verification exploited in the present study is the ECCI characterizations presented in Figs. 4 and 5 as well as later Figs. 11 and 12, in which stacking faults formation prevails at various deformation levels, while perfect dislocation glide is almost completely suppressed. Interestingly, while the P_{sf} in the present alloy is almost comparable to that of metastable HEAs which exhibit pronounced strain-induced FCC-to-HCP martensitic transformation [25,30], the resultant HCP-phase fraction, however, remains an order of magnitude lower. Since P_{sf}, by definition [78], also reflects the frequency of finding a deformation fault along the close packing 111 planes in FCC stacking sequence, a microstructure-related quantity, the average stacking fault distance, can also be determined as:

$$d_{sf} = d_{111}/P_{sf} \tag{4}$$

where d_{111} is the apparent spacing of 111 planes at a given deformation level. Along both axial and radial directions, the d_{sf} values demonstrate ~80 nm at a comparatively moderate strain level, followed by an evident decrease down to ~10 nm at the later stage of deformation (Fig. 8 (d)), complying with the qualitative trend revealed by ECCI analyses (Figs. 4 and 5). The associated strain hardening exponent ($n = \partial \ln\sigma^{true}/\partial \ln\varepsilon^{true}$), on the other hand, exhibits an eminent increase up to ~0.5 within the true strain realm of 0.0-20.0%, where the d_{sf} also witnesses the most pronounced reduction. This kind of latent correlation demonstrates the strain hardening contribution enabled by the faulting mechanism, for which a more detailed mechanistic consideration is provided in section 4.2.1.

4. Discussion

4.1. Intrinsic stacking fault energy in FCC-structured metastable alloys

4.1.1. Theoretical considerations

The activation of plastic deformation modules in bulk FCC-structured alloys, including perfect dislocation glide, mechanically-induced twinning or martensitic transformation has been well-documented to exhibit a close correlation to intrinsic stacking fault energy (γ_{iSFE}). From an atomistic standpoint, the γ_{iSFE} quantifies the propensity of nucleating an intrinsic stacking fault via dissociating a perfect $a/2\langle 110 \rangle$ dislocation into two paired $a/6\langle 112 \rangle$ glissile Shockley partials. The mobility and thereby the interactions amongst these partials serve as the operative unit in triggering deformation twinning or martensitic transformation. Thus far, numerous investigations of Al-, Cu-, and Fe-Mn-based alloys have rendered empirical indications [80,81] of the operating deformation module implied by the magnitude of γ_{iSFE}: (1) for comparatively low $\gamma_{iSFE} < 20\,mJ/m^2$, mechanically-induced FCC-HCP or FCC-HCP-body-centered tetragonal (BCT) martensitic transformation occurs; (2) for medium γ_{iSFE} in 20 ~ 40mJ/m^2 range, deformation twinning operates; and (3) for high $\gamma_{iSFE} > 40mJ/m^2$ perfect dislocation glide becomes predominant.

Unlike the foregoing three situations, the present $Co_{60}Cr_{25}Ni_{10}W_5$ CCA reveals an evident faulting response, which phenomenologically suggests that the formation of stacking faults should be the most effective micro-mechanism that enables energy dissipation during plastic deformation. Clearly, this sort of peculiar deformation response leads to a more dedicated assessment of the γ_{iSFE}. Since the present investigation was carried out at ambient temperature, and considering the fact that the chemical complexity may impede precise *ab-initio* calculations, we next assess the γ_{iSFE} in the viewpoint of thermodynamics. Structurally, the nucleation of a mono-layered intrinsic stacking fault in bulk FCC-crystals is in equivalent to creating an HCP stacking unit along with coherent FCC/HCP interfaces. The γ_{iSFE}, in this regard, is considered as the excess free-energy, according to the Olson-Cohen model [39]:

$$\gamma_{iSFE} = 2\rho_{111}\Delta G^{FCC \to HCP} + 2\sigma^{FCC/HCP} \tag{5}$$

where ρ_{111}, $\Delta G^{FCC \to HCP}$, and $\sigma^{FCC/HCP}$ respectively denote the atomic density of the 111 faulting plane, the Gibbs free-energy difference between FCC and HCP phases, and the coherent interfacial energy. Here, since $\rho_{111} = \frac{4}{\sqrt{3}}\frac{1}{a^2 N_A}$ and $\sigma^{FCC/HCP} \sim 7.5\,mJ/m^2$ for coherent interfaces [39] are both fixed constants, the only factor in Eq. (5) remains to be determined is the $\Delta G^{FCC \to HCP}$. Considering the chemical complexity of the present system, we estimate this quantity by adopting a sub-regular solution model [82,83]:

$$\Delta G_{total}^{FCC \to HCP} = \Delta G_{p.m.}^o + \Delta G^{ex.} \tag{6}$$

Here, $\Delta G_{p.m.}^o$ represents the Gibbs free-energy difference between FCC and HCP phases at the reference state, which takes the form of weighted average amongst all the alloying elements:

$$\Delta G_{p.m.}^o = \sum_i x_i \Delta G_i^{FCC \to HCP} \tag{7}$$

where x_i is the atomic fraction of the ith element and $\Delta G_i^{FCC \to HCP}$ the corresponding Gibbs free-energy difference between FCC and HCP structures. The total excess free energy term $\Delta G^{ex.}$ in Eq. (6) is modeled as the summation of binary ($\Delta G_{bin.}^{ex.}$) and ternary ($\Delta G_{tern.}^{ex.}$) interactive terms as well as the magnetic contribution ($\Delta G_{mag.}^{ex.}$):

$$\Delta G^{ex.} = \Delta G_{bin.}^{ex.} + \Delta G_{tern.}^{ex.} + \Delta G_{mag.}^{ex.} \tag{8}$$

To avoid redundancy in the main text, we have summarized all the analytical details of Eqs. (6)–(8) together with the excerption of physicochemical parameters in supplementary Note 1. The corresponding calculation results are illustrated as a function of temperature in Fig. 9 (a) and (b). Clearly, the $\Delta G_{total}^{FCC \to HCP}$ exhibits a negative quantity with a slight monotonic increase within the ambient temperature range (Fig. 9 (a)), suggesting the thermodynamically metastable feature of the present FCC-phase. Amongst all the constitutions considered in the sub-regular solution model, it is also recognized that the $\Delta G_{p.m.}^o$ term, which reflects the intrinsic ideal mixing tendency of the alloying elements, demonstrates the most predominant contribution. The higher order non-linear interactions, including $\Delta G_{bin.}^{ex.}$, $\Delta G_{tern.}^{ex.}$, and $\Delta G_{mag.}^{ex.}$, on the other hand, render comparatively minor effects. The resultant γ_{iSFE} calculated from Eq. (5) also reveals a negative value at ambient temperature (Fig. 9 (b)), reaching $-53.35\,mJ/m^2$ at 25 °C, being well accord with the ground state *ab-initio* prediction by Tian et al. [84] Notably, these calculation results seem contradictory with classical dislocation theory that persists an always positive γ_{iSFE}. We assert, however, negative γ_{iSFE} also exhibits a salient physical revelation, which will be detailed next from the perspectives of thermodynamics, structure, and mechanics.

Thermodynamically, according to Eq. (5), γ_{iSFE} is exactly the excess formation energy associated with the nucleation of stacking faults. Classically, a positive γ_{iSFE} implies that creation of a faulted 111 player in FCC stacking sequence will lead to free-energy elevation even after overcoming the kinetic energy barrier assisted by external loading [39]. This kind of free-energy increase will cease to be alleviated by the immediate formation of more stable bulk phase or structure in a sense to comply with the law of energy
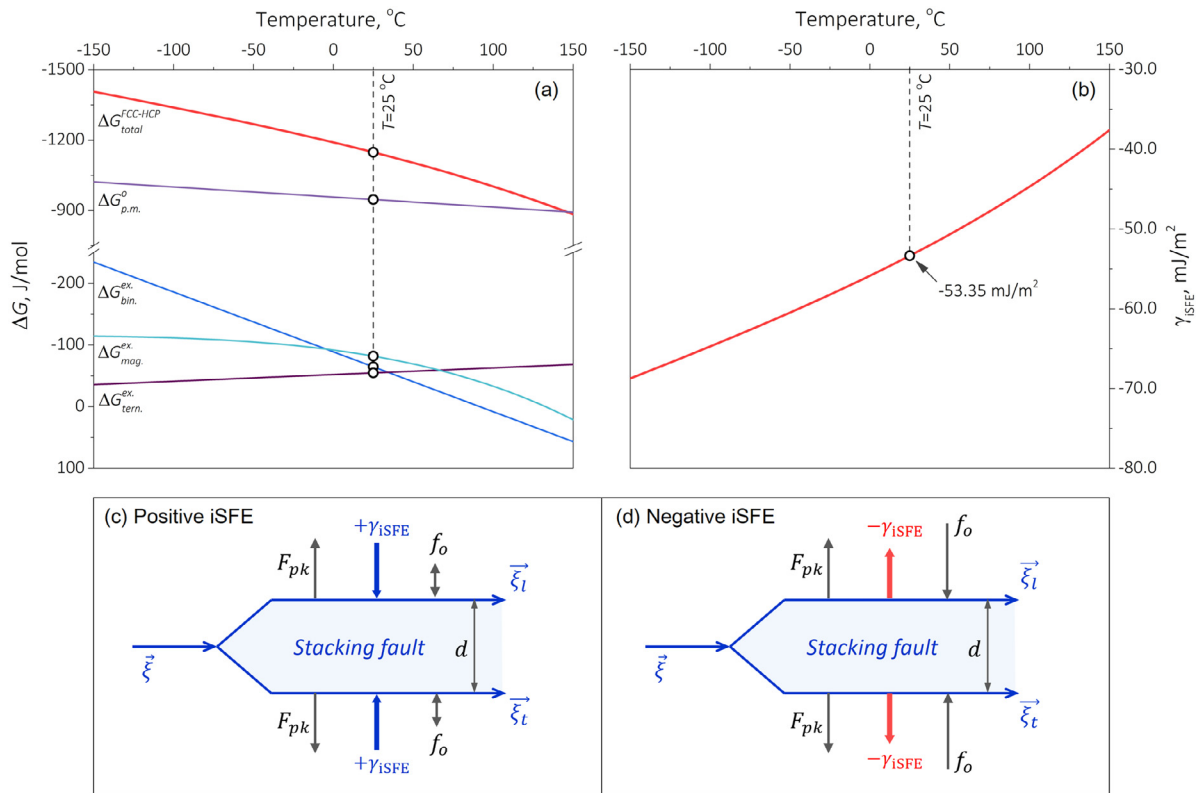
Fig. 9. Thermodynamic assessment of the $Co_{60}Cr_{25}Ni_{10}W_5$ CCA: (a) phase stability assessment in the sub-regular solution formalism (calculation details are referred to supplementary Note 1); (b) estimation of intrinsic stacking fault energy as a function of temperature; (c) and (d) stress-free equilibrium considering positive and negative intrinsic stacking fault energies.

dissipation for plasticity. As such, creation of mono-layered stacking faults (namely, deformation faulting) can barely become predominant in the plastic deformation for alloys that exhibit positive γ_{iSFE}. Instead, features like HCP-martensite or twins, whose formation can be aided by stacking faults will become prevalent, and this, as discussed earlier, has been well-verified in classical Fe-Mn-based alloys. A negative γ_{iSFE}, on the other hand, suggests that the faulted 111 layer is more energetically favorable than the perfect FCC stacking sequence. That stated, mechanically nucleating even a mono-layered stacking fault is already a micro-plasticity event that dissipates strain energy. Under this energetic framework, it is expected that extensive amounts of uncorrelated stacking faults can become thermodynamically stable in the plastic realm, microscopically giving rise to the deformation faulting response as demonstrated in Figs. 4, 5, and 8. Only at comparatively higher deformation levels, i.e. when the energy dissipation caused by individual faulting unit can no longer compensate the free-energy increase due to the interaction amongst the stacking faults (see Section 4.2.1), will the formation of other bulk structures start to take place. This is also the phenomenological reason why compared to the Fe-Mn-based alloys with positive γ_{iSFE}, blocky HCP-martensite nucleation in the present $Co_{60}Cr_{25}Ni_{10}W_5$ CCA is significantly delayed (Fig. 7 (e)).

Structurally, the proposition that needs to be addressed is whether or not the extended dislocation still complies with the stress-free equilibrium criterion in light of a negative γ_{iSFE}? As schematically shown in Fig. 9 (c) and (d), such a structure consists of one layer of stacking fault enclosed by a leading ($\vec{\xi}_l$) and a trailing ($\vec{\xi}_t$) glissile Shockley partial that dissociate from a perfect dislocation ($\vec{\xi}$). Since the elastic strain energy in the FCC crystal, according to the Frank's criterion [29], is alleviated by the creation of Shockley partials, the underlying Peach-Koehler interaction al-

ways results in a repulsive force ($F_{pk} \propto 1/r$, r is the separation distance) between two paired partials. In the case of positive γ_{iSFE} (Fig. 9 (c), for most stable FCC alloys), as the creation of a stacking fault leads to free-energy increase, the resultant interactive effect gives rise to an attractive force, tending to shrink the stacking fault. By presuming that the lattice frictional force (f_o) is negligibly small, the stress-free equilibrium is therefore achieved between the repulsive Peach-Koehler force and the attractive force originating from the stacking fault, enabling an equilibrium stacking fault width (d) [29]:

$$d = \frac{G}{2\pi \gamma_{iSFE}} \left[\left(\vec{b}_l \cdot \vec{\xi}_l \right)\left(\vec{b}_t \cdot \vec{\xi}_t \right) + \frac{\left(\vec{b}_l \times \vec{\xi}_l \right)\left(\vec{b}_t \times \vec{\xi}_t \right)}{1 - \nu} \right] \quad (9)$$

where, $\vec{b}_l$ and $\vec{b}_t$ are the Burgers vectors of the leading and the trailing partials, G and ν denoted the shear modulus and the Poisson's ratio of the alloy. Practically, Eq. (9) has also witnessed broad applications in determining γ_{iSFE} via high-resolution TEM experimentation [35,85–87]. In the case of negative γ_{iSFE} (Fig. 9 (d)), by contrast, a repulsive force is then associated with the formation of stacking fault, exhibiting the trend to extend its width. Critically, the stress-free equilibrium described by Eq. (9) breaks down. However, as seen in the experimental results in Figs. 4 and 5 (and later Figs. 10 and 11), stacking fault structures do reach mechanical equilibrium even when the external load is removed. We therefore assert that in metastable FCC alloys with negative γ_{iSFE}, it is the lattice frictional force that serves to balance the foregoing two repulsive forces, preserving the finite partial separation width. While a quantitative validation of such a hypothesis for the current CCA deems dedicated modeling effort, previous theoretical investigation by Baudouin et al. [88] does confirm the significant role of lattice frictional force in the equilibrium stacking fault width. It is worth-
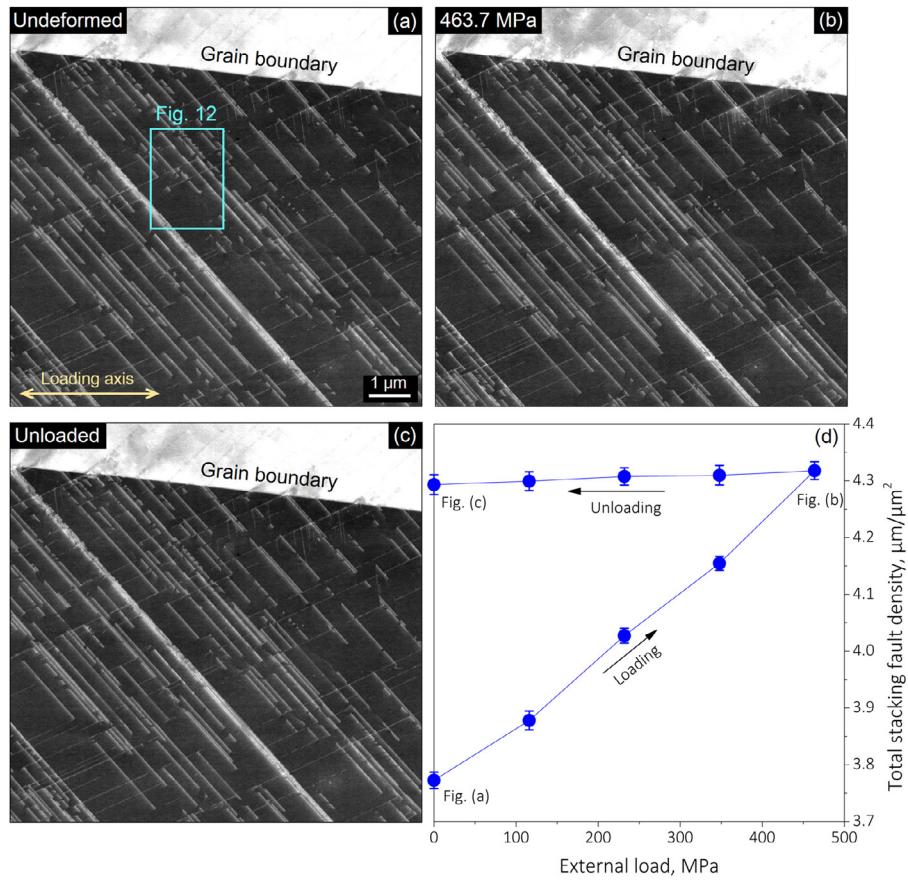
Fig. 10. Statistical examination of stacking fault density change during one elastic tension loading-unloading cycle: (a)-(c) *in-situ* ECCI micrographs acquired at undeformed, maximum stress, and unloaded states (the same scale bar is applied); (d) the corresponding stacking fault density change. Extended experimental details are provided in supplementary Fig. S7-S9.
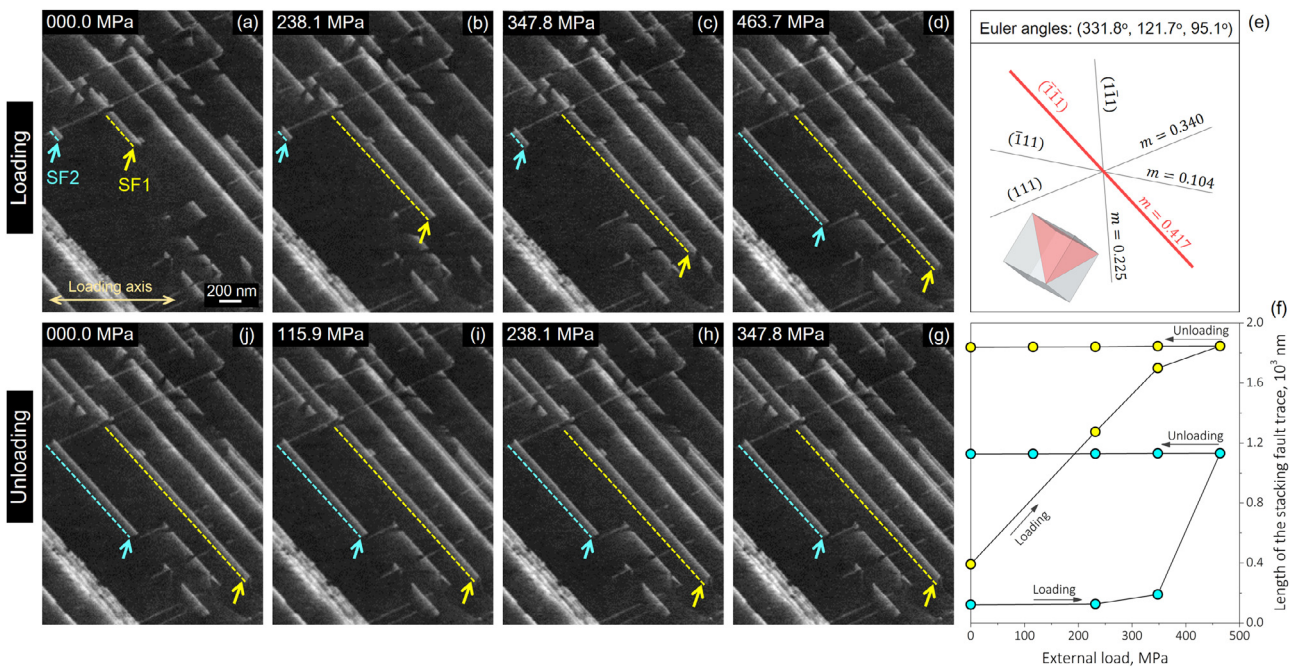

Fig. 11. *In-situ* ECCI analysis of local stacking fault activity: (a)-(d) elastic loading; (g)-(j) unloading; (e) faulting plane trace and the corresponding Schmid factor for the selected region (calculation details are referred to supplementary Note 2); (f) stacking fault length change during one loading-unloading cycle. The same scale bar is applied in (a)-(d) and (g)-(j).

while noting that γ_{iSFE} determination of metastable FCC alloys on the theoretical basis of Eq. (9) or its variations may largely deviate from the actual scenario, leading to contradictory explanations of the operative deformation micro-mechanisms.

Mechanically, the negative γ_{iSFE} is of fundamental significance, straightforwardly in the viewpoint of generalized stacking fault energy (GSFE) [89,90], or more broadly, the deformation energy landscape [91]. The essence of GSFE lies in the description of energy change per unit area upon shearing a certain crystal along an intended strain path [89]. As such, the resultant energy-atomistic displacement curve, if achieved along the $\{111\}\langle112\rangle$ path, measures the energy landscape of nucleating a partial dislocation, along which the energy corresponds to $|a/6\langle112\rangle|$ is the γ_{iSFE} discussed above. Under this theoretical framework, a negative γ_{iSFE} thus implies: (1) operation of partial dislocation glide becomes predominant; (2) after overcoming an energy barrier, namely the unstable stacking fault energy γ_{uSFE}, the faulted crystal becomes more stable compared to its defect-free counterpart, being compatible with the thermodynamic understanding; and (3) successive creation of stacking faults (in equivalent to correlated mono-layered HCP stacking) will tend to destabilize the original metastable FCC structure, giving rise to the formation of HCP-phase. It is worthwhile noting that, coinciding with the foregoing thermodynamic calculation (Fig. 9 (b)), ground state GSFE computation [84] of individual alloying effect for Ni, Cr, or W in a Co-matrix all demonstrates negative γ_{iSFE} with less 50 at.% content, which is supportive of both the observed deformation substructures (Figs. 4 and 5) and the metastability nature of the present alloy. Still, as implied by the GSFE formalism, whether or not faulting can become the most predominant deformation micro-mechanism also relies on the energy barrier term (γ_{uSFE}). A more recent simulation work by Jo et al. [92] proposed $\gamma_{iSFE}/(\gamma_{iSFE} - \gamma_{uSFE})$ as an inherent indicator for the operative deformation module, in which a nominally negative value signifies the occurrence of significant faulting event, being consistent with our experimental observation. From a continuum mechanics perspective, such a latent correlation has also been established via the classical dislocation theory, according to Lagerlof et al. [93]:

$$\tau_c = \frac{2\alpha Gb_p}{D} + \gamma_{iSFE}/b_p \qquad (10)$$

here, τ_c is represents the critical resolved stress for nucleating a glissile Shockley partial ($\tau_c \sim |\nabla\gamma|_{max}$ in the viewpoint of GSFE) which is an explicit function of dislocation category (α), shear modulus (G), grain size (D), magnitude of Burgers vector (b_p), and γ_{iSFE}. Evidently, a negative γ_{iSFE} exhibits the trend to mitigate τ_c, which in turn facilitates the nucleation of partial dislocations.

4.1.2. Experimental verifications

By clarifying the thermodynamic, structural, and mechanical implications of negative γ_{iSFE}, we now propose the following three assertions regarding the deformation response for metastable FCC alloys with significantly negative γ_{iSFE}: (1) compared with perfect dislocation glide, operation of glissile Shockley partials becomes predominant, giving rise to deformation faulting; (2) the extension of stacking fault via the emission of glissile partials exhibits a mechanically irreversible characteristic; and (3) the bulk FCC phase will demonstrate a somewhat metastable feature, but the formation of blocky-HCP structure is presumably delayed.

The foregoing postulates (1) and (3) can be naturally deduced from the structural and thermodynamic discussion proposed above, and their validity has already been confirmed in the Results section. Intriguingly, the second postulate which is drawn from a thermodynamic-mechanical aspect, enables the design of an *in-situ* ECCI experiment for validation. The experiment consists of assessing the variation in stacking fault length during elastic tension

loading-unloading cycle, intended to examine whether or not the creation of stacking faults is indeed an energetically favored micro-event as dictated by the negative γ_{iSFE} and Eq. (5).

As discussed earlier, while *in-situ* mechanical testing coupled with ECCI enables the elucidation of deformation substructure evolution with a broader view-of-field, potential artifacts or inaccuracies in the proceeding investigation may potentially arise from three major respects: (1) tensile stage or sample tilting can alter the imaging condition, causing an overestimation of stacking fault density, which is owing to the variation in channeling contrast; (2) the polycrystallinity nature of the investigated alloy can render heterogeneous local stress distribution, leading to the deviation from global stress state, which in turn diversifies the local stacking fault activity; and (3) interstitial elements can give rise to Suzuki segregation [29,94], also contributing to the irreversible extension of the stacking fault. For (1), we have revealed in supplementary Fig. S7 and S8 the systematic error calibration results, proving that any possible sample misalignment or tilting within $\pm 1.5^o$ will only lead to the underestimation of stacking fault density. For (2), we will combine the statistical assessment of stacking fault density change at the length-scale of grain size (Fig. 10) and the representative local stacking fault activity (Fig. 11) so as to ensure the reliability of the results. For (3), since the present alloy consists of purely substutional elements and tensile testing results in Fig. 3 confirm the absence of Portevin-Le Chatelier band [95] or yield-dropping [96], it is therefore suggestive that the effect of interstitial atoms on the corresponding mechanical response is negligible.

Fig. 10 reveals the global statistical assessment of stacking fault density change upon one elastic loading-unloading cycle. Here, stacking faults were introduced into the specimen by applying a ~2.0% pre-strain (corresponding engineering stress is ~577 MPa, supplementary Fig. S9), then the surface steps were removed by metallographic polishing to enable ECCI characterization. The maximum stress level reached in the loading-unloading experiment was controlled as 463.7 MPa, being well below the macroscopic yielding point. Note that in the present statistical analysis, we determine the stacking fault density (ρ_{sf}), as the length of the plane traces per unit observational area ($A_{obv.}$):

$$\rho_{sf} = \frac{\sum length\ of\ the\ stacking\ fault\ traces}{A_{obv.}} \qquad (11)$$

At the undeformed state (Fig. 10 (a)), the total ρ_{sf} achieves 3.77 $\mu m/\mu m^2$ (due to pre-strain), which then witnesses a monotonic increasing trend with respect to elevating stress level, reaching up to 4.31 $\mu m/\mu m^2$ at 463.7 MPa applied stress (Fig. 10 (b)). During the unloading portion of the experiment, the total ρ_{sf} reveals an almost invariant characteristic regardless of the removal of the external load to various extents (Fig. 10 (d)). The corresponding ρ_{sf} at the fully unloaded state (Fig. 10 (c)) maintains 4.29 $\mu m/\mu m^2$. These results suggest that in line with the assertion (2) proposed earlier, the stacking fault extension in the present alloy does reveal an irreversible nature from a global perspective, supporting the characteristic of a negative γ_{iSFE}. To more comprehensively assess the stacking fault activity, we next focus on the local behavior of two stacking fault ribbons during the foregoing elastic loading-unloading cycle.

It is recognized from crystallographic calculations (details see supplementary Note 2) that the two stacking fault ribbons (marked with yellow and cyan arrows in Fig. 11 (a)) investigated here both belong to the $(\bar{1}\bar{1}1)$ faulting plane (Fig. 11 (e)), with a maximum Schmid factor (m) of 0.417 for the corresponding glissile partials (calculation details are presented in supplementary Note 2). At the undeformed state, the length of their traces respective achieves 391.3 (yellow, SF1) and 122.3 nm (cyan, SF2). As the applied stress level increases to 238.1 MPa, SF1 undergoes a no-
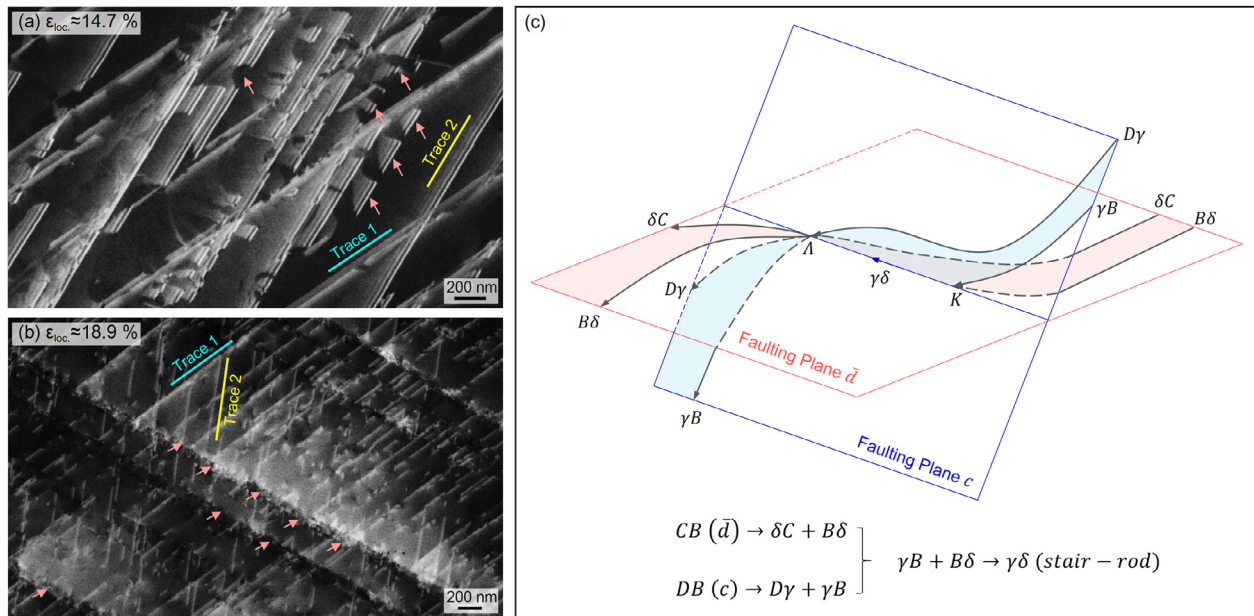
Fig. 12. ECCI micrographs for representative unparallel stacking faults: (a) shattered stacking faults (local stain level ~14.7%); (b) local pinning spots at the junctions between stacking faults (local strain level ~18.9%); (c) schematic of the dislocation reaction associated with the intersected stacking fault ribbons.

ticeable extension in its trace length, reaching 231.8 nm (Fig. 11 (b)). Such a monotonic increasing trend keeps on evolving as the applied stress elevates (Fig. 11 (b)-(d)), and its eventual length achieves 1845.3 nm towards the end of the loading half-cycle (Fig. 11 (d) and (f)), which is approximately 5 times the length of the undeformed state. SF2 also witnesses a similarly monotonic increase in its length (Fig. 11 (a)-(d) and (f)), exhibiting 1131.3 nm at 463.7 MPa applied stress. When the external load is gradually removed (Fig. 11 (g)-(j)), both SF1 and SF2 preserve their lengths regardless of the deceasing stress level, and no discernable shrinkage within the faulted region is detected, again validating the irreversible extension hypothesis. It should be noted that the present results are of distinctive contrast when compared with a most recent report by Habib et al. [97] in an Fe-Cr-N steel with a widely-documented [98,99] positive γ_{iSFE}, in which evident reversible extension of the stacking faults was revealed by *in-situ* ECCI characterizations. Thus far, the global statistical assessment along with the local stacking fault activity investigation compatibly verifies the foregoing assertion (2) drawn from the physical foundations of negative γ_{iSFE}.

4.2. Strain hardening micro-mechanisms and insights into metastable CCAs/HEAs development

4.2.1. Hardening via faulting

As typical planar defects in crystalline solids, stacking faults have been documented to render substantial strengthening effect particularly in light of their interaction with glissile perfect dislocations. Exemplary experimental investigations of Cu-Al dilute alloys [100] and CoCrNiFeNb concentrated alloys [37], as well as molecular dynamics (MD) simulation [101], all verify that the presence of stacking faults can significantly impede the perfect dislocations from crossing the faulting plane, which in turn leads to stress elevation. In the foregoing regards, physical analogy of stacking faults is largely taken as grain or twin boundaries, in which the spacing between them is considered as the mean free path for glissile perfect dislocations [102], and as such, the classical Hall-Petch-like concept is often applied to elucidate the strain hardening contribution [100,103–105]. Contradictorily, both *in-situ* and

post-mortem ECCI characterizations confirm the negligible content of perfect dislocations in the present $Co_{60}Cr_{25}Ni_{10}W_5$ CCA (Fig. 4 and 11), leading to a more detailed consideration of the underlying strain hardening micro-mechanisms. By closely examining the deformation substructures by ECCI, we propose (1) the intersection between unparallel stacking faults which leads to the formation of sessile dislocations; and (2) the elastic repulsion between parallel stacking faults to be the two mechanistic origins that enable strain hardening.

Fig. 12 (a) and (b) present the stacking fault structures at local strain levels of ~14.7% and ~18.9%. At these deformation levels, it is revealed by ECCI micrographs that stacking faults belong to unparallel {111} faulting planes are nucleated (marked as trace 1 and 2), and exhibit the trend to intersect with one another. Evident node-like features can be clearly observed along the intersected regions, which are characterized by the shattered stacking fault ribbons (marked with pink arrows in Fig. 12 (a)). This kind of node structures, if consider the unparallel geometry of the activated faulting system, can be reasonably ascribed to the reaction amongst the glissile partials. Following the Thompson tetrahedron convention [29], we sketch one such possibility in Fig. 12 (c). Owing to the negative γ_{iSFE} in the present $Co_{60}Cr_{25}Ni_{10}W_5$ CCA, perfect dislocations CB and DB dissociate into glissile Shockley partials following plastic incipience respectively via: $CB \rightarrow \delta C + B\delta$ and $DB \rightarrow D\gamma + \gamma B$ on the corresponding faulting plane $\bar{d}$ and c. As the stacking faults extend due to the increase of applied stress, reaction between partials γB and $B\delta$ takes place, leading to the formation of a stair-rod sessile partial $\gamma\delta$, jamming along the intersection between faulting plane $\bar{d}$ and c. Since the Burgers vector of edge dislocation $\gamma\delta$ yields $a/6[110]$, whose glide plane is neither $\bar{d}$ nor c, a strong Lomer-Cottrell locking effect [106] is therefore expected to occur at the intersection ΛK, effectively contributing to strain hardening and simultaneously giving rise to the node-like structures associated with shattered faults in Fig. 12 (a) as well as the localized pinning spots in Fig. 12 (b). We note that although the foregoing analysis considers a Lomer-Cottrell locking mechanism, which from the standpoint of Frank's energy criterion [29], enables the most significant energy dissipation, other similar micro-event, especially Hirth locking has also been proved to

possess exceptional strain hardenability according to MD simulation [71], its energy dissipation rate, however, is comparatively less pronounced. In addition, while jogs formation from the reaction between partially associated unparallel stacking faults may also contribute to strain hardening [107,108], the negative γ_{iSFE} and thereby the irreversible formation of the stacking faults (Fig. 11) in the present CCA would significantly retard the association procedure, rendering this mechanism less probable to occur. However, more quantitative elucidation of the corresponding energy landscape deems further simulation effort.

The parallel stacking faults that belong to the same {111} plane, on the other hand, can also lead to strain hardening via the elastic interaction between one another. Especially at the early stage of plastic deformation (Fig. 4 (a) and (b)), faulting activity tends to be compatible with the Schmid's law, which consequently leads to the parallel alignment of stacking faults. Under this geometric framework, and if individual faulting unit can be presumed to be uncorrelated, nucleation and thereby extension of one stacking fault layer in between two existing ones will witness an extra elastic repulsive force due to the Peach-Koehler interaction between glissile partials. The magnitude for this sort of elastic interaction, according to classical dislocation theory [29], increases inversely proportional to the distance between parallel stacking fault ribbons (as their fraction increases due to the elevation of applied stress, Fig. 8 (c) and (d)), providing strain hardening even in the absence of the foregoing sessile dislocation locking event. Because of its intrinsically elastic nature, it should be noted that this kind of parallel stacking fault-induced strain hardening mechanism should, in principle, be ubiquitous in any metallic alloys where deformation faulting can become predominant.

4.2.2. Considerations of metastable CCAs/HEAs design strategy

Comparison between the present $Co_{60}Cr_{25}Ni_{10}W_5$ CCA and the latest metastable FeMnCoCr HEAs evidently reveals the improved strength-ductility synergy due to the operation of extensive deformation faulting response (Fig. 3 (a) and 7 (e)). Although the strain-induced FCC-HCP martensitic transformation within the latter also promotes strain hardenability, its mechanistic limitation largely associates with the blocky HCP-martensite because: (1) limited slip system and pronounced plastic anisotropy of the HCP-structure retard effective plastic strain accommodation [109,110]; and (2) strain incompatibility occurring at the junction between HCP-martensite and FCC grain boundaries immediately facilitates micro-cracking [111]. A micro-mechanical revelation of this dilemma can be understood from the fact that blocky HCP-phase formation is a procedure that renders almost complete exhaustion of "local ductility" [112], sacrificing the capability of delocalizing any stress concentrator onwards. Mechanistically, it can be therefore deduced that if individual HCP-band can be ideally refined to infinitely thin and remains thermodynamically stable, the foregoing "local ductility" exhaustion dilemma can be potentially mitigated. Intriguingly, as discussed in Section 4.1.1, such an idealized scenario is feasibly achieved by the present deformation faulting response (see structural consideration in 4.1.1), and the corresponding γ_{iSFE} ensures the thermodynamic stability of the stacking faults (see thermodynamic consideration in 4.1.1). In the theoretical framework of microstructural metastability engineering, we note that complete tunable design of faulting CCAs/HEAs may not only rely on negative γ_{iSFE}, but also requires mechanical stability of the stacking faults. In this regard, it is therefore suggestive that multi-layered GSFE computation [91] is indispensable in elucidating the full deformation energy landscape, especially considering the correlation between individual faulting unit and the mechanical energy barrier for HCP-phase as well as mechanical twin nucleation. As such, we assert that in addition to the profuse focus on strain-induced martensitic transformation or mechanical twinning, de-

formation faulting, or ideally speaking, faulting-mediated plasticity can also become a mechanistically-driven design strategy for advancing metastable CCAs/HEAs development.

5. Conclusions

With the aids of *in-situ* synchrotron X-ray diffractometry and *in-situ* ECCI technique, we have systematically explored the deformation micro-mechanisms of a metastable $Co_{60}Cr_{25}Ni_{10}W_5$ CCA with primary focus on the role of stacking faults, and major findings are concluded in the following respects:

(1) In contrast to perfect dislocation glide or strain-induced FCC-HCP martensitic transformation, it is recognized that the nucleation and thereby multiplication of stacking faults is acting as the major plasticity carrier in the present CCA. Results of *in-situ* synchrotron X-ray diffraction experiment validate a direct correlation between the increase of stacking fault probability and the elevation of strain hardening exponent, indicating that the deformation faulting mechanism by itself enables macroscopic strain hardening;

(2) By quantitatively exploring the relative phase stability through thermodynamic modeling, we show that this sort of less-explored deformation faulting response is mechanistically related to a negative intrinsic stacking fault energy. Its physical foundations are theoretically assessed in the aspects of thermodynamics, structure, and mechanics, supported by *in-situ* ECCI analyses which verify the irreversible extension of stacking faults during elastic loading-unloading cycle;

(3) Unlike the classical Hall-Petch-type concept which ascribes strain hardening to stacking fault-glissile perfect dislocation interaction, we reveal that in the absence of perfect dislocations, two micro-events are essential in rendering strain hardenability, namely, the nucleation of sessile dislocation via intersected unparallel stacking faults and the elastic repulsion between parallel stacking faults;

(4) Through the comparison between the present CCA and the metastable FeMnCoCr-type HEAs where strain-induced FCC-HCP martensitic transformation is predominant, it is suggestive that the present deformation faulting micro-mechanism can effectively alleviate the drastic exhaustion of local ductility in the latter case, demonstrating the potential in avoiding early-stage damage nucleation. We also note that future simulation effort aiming at the elucidation of the entire deformation energy landscape would expedite the mechanistically-driven metastable CCAs/HEAs design, magnifying the benefits of deformation faulting response.

Declaration of Competing Interest

The authors declare that they have no known competing financial interests or personal relationships that could have appeared to influence the work reported in this paper.

Supplementary materials

Supplementary material associated with this article can be found, in the online version, at doi:10.1016/j.actamat.2020.09.056.

References

[1] B. Cantor, I.T.H. Chang, P. Knight, A.J.B. Vincent, Microstructural development in equiatomic multicomponent alloys, Mater. Sci. Eng. A. 375–377 (2004) 213–218 https://doi.org/10.1016/j.msea.2003.10.257.

[2] J.W. Yeh, S.K. Chen, S.J. Lin, J.Y. Gan, T.S. Chin, T.T. Shun, C.H. Tsau, S.Y. Chang, Nanostructured high-entropy alloys with multiple principal elements: novel alloy design concepts and outcomes, Adv. Eng. Mater. 6 (2004) 299–303, doi:10.1002/adem.200300567.

[3] D.B. Miracle, O.N. Senkov, A critical review of high entropy alloys and related concepts, Acta Mater. 122 (2017) 448–511, doi:10.1016/J.ACTAMAT.2016.08.081.

[4] Z. Lei, Y. Wu, J. He, X. Liu, H. Wang, S. Jiang, L. Gu, Q. Zhang, B. Gault, D. Raabe, Z. Lu, Snoek-type damping performance in strong and ductile high-entropy alloys, Sci. Adv. (2020), doi:10.1126/sciadv.aba7802.

[5] S. Wei, S.J. Kim, J.Y. Kang, Y. Zhang, Y. Zhang, T. Furuhara, E.S. Park, C.C. Tasan, Natural-mixing guided design of refractory high-entropy alloys with as-cast tensile ductility, Nat. Mater. (2020), doi:10.1038/s41563-020-0750-4.

[6] U. Sydney, A. Hohenwarter, D. Catoor, E.H. Chang, E.P. George, R.O. Ritchie, A fracture-resistant high-entropy alloy for cryogenic applications, Science 345 (2014) 1153–1159 (80-)., doi:10.1126/science.1254581.

[7] Y.H. Jo, S. Jung, W.M. Choi, S.S. Sohn, H.S. Kim, B.J. Lee, N.J. Kim, S. Lee, Cryogenic strength improvement by utilizing room-temperature deformation twinning in a partially recrystallized VCrMnFeCoNi high-entropy alloy, Nat. Commun. (2017), doi:10.1038/ncomms15719.

[8] Q. Ding, Y. Zhang, X. Chen, X. Fu, D. Chen, S. Chen, L. Gu, F. Wei, H. Bei, Y. Gao, M. Wen, J. Li, Z. Zhang, T. Zhu, R.O. Ritchie, Q. Yu, Tuning element distribution, structure and properties by composition in high-entropy alloys, Nature (2019), doi:10.1038/s41586-019-1617-1.

[9] O.N. Senkov, G.B. Wilks, J.M. Scott, D.B. Miracle, Mechanical properties of Nb25Mo25Ta25W25 and V20Nb20Mo20Ta20W20 refractory high entropy alloys, Intermetallics 19 (2011) 698–706.

[10] F. Maresca, W.A. Curtin, Mechanistic origin of high strength in refractory BCC high entropy alloys up to 1900K, Acta Mater. (2020), doi:10.1016/j.actamat.2019.10.015.

[11] O.N. Senkov, D.B. Miracle, K.J. Chaput, J.-P. Couzinie, Development and exploration of refractory high entropy alloys—A review, J. Mater. Res. (2018) 1–37, doi:10.1557/jmr.2018.153.

[12] F. He, D. Chen, B. Han, Q. Wu, Z. Wang, S. Wei, D. Wei, J. Wang, C.T. Liu, J. Kai, Design of D022 superlattice with superior strengthening effect in high entropy alloys, Acta Mater. (2019), doi:10.1016/J.ACTAMAT.2019.01.048.

[13] B. Gwalani, S. Gangireddy, Y. Zheng, V. Soni, R.S. Mishra, R. Banerjee, Influence of ordered L1 2 precipitation on strain-rate dependent mechanical behavior in a eutectic high entropy alloy, Sci. Rep. (2019), doi:10.1038/s41598-019-42870-y.

[14] N. Gao, D.H. Lu, Y.Y. Zhao, X.W. Liu, G.H. Liu, Y. Wu, G. Liu, Z.T. Fan, Z.P. Lu, E.P. George, Strengthening of a CrMnFeCoNi high-entropy alloy by carbide precipitation, J. Alloys Compd. (2019), doi:10.1016/j.jallcom.2019.04.121.

[15] C. Zhang, C. Zhu, T. Harrington, K. Vecchio, Design of non-equiatomic high entropy alloys with heterogeneous lamella structure towards strength-ductility synergy, Scr. Mater. (2018), doi:10.1016/j.scriptamat.2018.05.020.

[16] E.P. George, D. Raabe, R.O. Ritchie, High-entropy alloys, Nat. Rev. Mater. (2019), doi:10.1038/s41578-019-0121-4.

[17] E.J. Pickering, R. Muñoz-Moreno, H.J. Stone, N.G. Jones, Precipitation in the equiatomic high-entropy alloy CrMnFeCoNi, Scr. Mater. 113 (2016) 106–109, doi:10.1016/j.scriptamat.2015.10.025.

[18] F. He, Z. Wang, Q. Wu, J. Li, J. Wang, C.T. Liu, Phase separation of metastable CoCrFeNi high entropy alloy at intermediate temperatures, Scr. Mater. 126 (2017) 15–19 http://dx.doi.org/10.1016/j.scriptamat.2016.08.008.

[19] F. Otto, A. Dlouhý, K.G. Pradeep, M. Kuběnová, D. Raabe, G. Eggeler, E.P. George, Decomposition of the single-phase high-entropy alloy CrMnFeCoNi after prolonged anneals at intermediate temperatures, Acta Mater. (2016), doi:10.1016/j.actamat.2016.04.005.

[20] S. Wei, F. He, C.C. Tasan, Metastability in high-entropy alloys: A review, J. Mater. Res. 33 (2018) 2924–2937, doi:10.1557/jmr.2018.306.

[21] Z. Li, K.G. Pradeep, Y. Deng, D. Raabe, C.C. Tasan, Metastable high-entropy dual-phase alloys overcome the strength-ductility trade-off, Nature 534 (2016) 227–230, doi:10.1038/nature17981.

[22] Z. Li, S. Zhao, R.O. Ritchie, M.A. Meyers, Mechanical properties of high-entropy alloys with emphasis on face-centered cubic alloys, Prog. Mater. Sci. (2019), doi:10.1016/j.pmatsci.2018.12.003.

[23] S. Chen, H.S. Oh, B. Gludovatz, S.J. Kim, E.S. Park, Z. Zhang, R.O. Ritchie, Q. Yu, Real-time observations of TRIP-induced ultrahigh strain hardening in a dual-phase CrMnFeCoNi high-entropy alloy, Nat. Commun. (2020), doi:10.1038/s41467-020-14641-1.

[24] W. Lu, C.H. Liebscher, G. Dehm, D. Raabe, Z. Li, Bidirectional transformation enables hierarchical nanolaminate dual-phase high-entropy alloys, Adv. Mater. 30 (2018) 1–10, doi:10.1002/adma.201804727.

[25] S. Wei, J. Kim, J.L. Cann, R. Gholizadeh, N. Tsuji, C.C. Tasan, Plastic strain-induced sequential martensitic transformation, Scr. Mater. 185 (2020) 36–41, doi:10.1016/j.scriptamat.2020.03.060.

[26] W.G. Nöhring, W.A. Curtin, Cross-slip of long dislocations in FCC solid solutions, Acta Mater (2018), doi:10.1016/j.actamat.2018.05.027.

[27] B. Wang, H. He, M. Naeem, S. Lan, S. Harjo, T. Kawasaki, Y. Nie, H.W. Kui, T. Ungár, D. Ma, A.D. Stoica, Q. Li, Y. Ke, C.T. Liu, X.L. Wang, Deformation of CoCrFeNi high entropy alloy at large strain, Scr. Mater. (2018), doi:10.1016/j.scriptamat.2018.06.013.

[28] T.M. Smith, M.S. Hooshmand, B.D. Esser, F. Otto, D.W. Mccomb, E.P. George, M. Ghazisaeidi, M.J. Mills, Atomic-scale characterization and modeling of 60°dislocations in a high-entropy alloy, Acta Mater. (2016), doi:10.1016/j.actamat.2016.03.045.

[29] P.M. Anderson, J.P. Hirth, J. Lothe, Theory of dislocations, 3rd Edition, 2017.

[30] S.F. Liu, Y. Wu, H.T. Wang, W.T. Lin, Y.Y. Shang, J.B. Liu, K. An, X.J. Liu, H. Wang, Z.P. Lu, Transformation-reinforced high-entropy alloys with superior mechanical properties via tailoring stacking fault energy, J. Alloys Compd. 792 (2019) 444–455, doi:10.1016/j.jallcom.2019.04.035.

[31] M. Frank, Y. Chen, S.S. Nene, S. Sinha, K. Liu, K. An, R.S. Mishra, Investigating the deformation mechanisms of a highly metastable high entropy alloy using in-situ neutron diffraction, Mater. Today Commun. (2020), doi:10.1016/j.mtcomm.2019.100858.

[32] D. Wei, X. Li, S. Schönecker, J. Jiang, W.M. Choi, B.J. Lee, H.S. Kim, A. Chiba, H. Kato, Development of strong and ductile metastable face-centered cubic single-phase high-entropy alloys, Acta Mater (2019), doi:10.1016/j.actamat.2019.09.050.

[33] Q.J. Li, H. Sheng, E. Ma, Strengthening in multi-principal element alloys with local-chemical-order roughened dislocation pathways, Nat. Commun. (2019), doi:10.1038/s41467-019-11464-7.

[34] B. Yin, S. Yoshida, N. Tsuji, W.A. Curtin, Yield strength and misfit volumes of NiCoCr and implications for short-range-order, Nat. Commun. (2020), doi:10.1038/s41467-020-16083-1.

[35] R. Zhang, S. Zhao, J. Ding, Y. Chong, T. Jia, C. Ophus, M. Asta, R.O. Ritchie, A.M. Minor, Short-range order and its impact on the CrCoNi medium-entropy alloy, Nature (2020), doi:10.1038/s41586-020-2275-z.

[36] Y.L. Zhao, T. Yang, Y. Tong, J. Wang, J.H. Luan, Z.B. Jiao, D. Chen, Y. Yang, A. Hu, C.T. Liu, J.J. Kai, Heterogeneous precipitation behavior and stacking-fault-mediated deformation in a CoCrNi-based medium-entropy alloy, Acta Mater (2017), doi:10.1016/j.actamat.2017.07.029.

[37] F. He, Z. Wang, Q. Wu, D. Chen, T. Yang, J. Li, J. Wang, C.T. Liu, J. Jung Kai, Tuning the defects in face centered cubic high entropy alloy via temperature-dependent stacking fault energy, Scr. Mater. (2018), doi:10.1016/j.scriptamat.2018.06.002.

[38] G.B. Olson, M. Cohen, Kinetics of strain induced martensitic nucleation, Metall. Trans. A. 6 A (1975) 791–795, doi:10.1007/BF02672301.

[39] G.B. Olson, M. Cohen, A general mechanism of martensitic nucleation, Metall. Trans. A. 7 (1976) 1897–1904, doi:10.1007/BF02659822.

[40] G.B. Olson, M. Cohen, A mechanism for the strain-induced nucleation of martensitic transformations, J. Less-Common. Met. 28 (1972) 107–118, doi:10.1016/0022-5088(72)90173-7.

[41] O. Blaschko, G. Krexner, J. Pleschiutschnig, G. Ernst, C. Hitzenberger, H.P. Karnthaler, A. Korner, Coherent modulated structure during the martensitic hcp-fcc phase transition in Co and in a CoNi alloy, Phys. Rev. Lett. 60 (1988) 2800–2803, doi:10.1103/PhysRevLett.60.2800.

[42] P. Tolédano, G. Krexner, M. Prem, H.P. Weber, V.P. Dmitriev, Theory of the martensitic transformation in cobalt, Phys. Rev. B - Condens. Matter Mater. Phys. (2001), doi:10.1103/PhysRevB.64.144104.

[43] Y. Chen, Y. Li, Y. Koizumi, H. Haider, A. Chiba, Effects of carbon addition on wear mechanisms of CoCrMo metal-on-metal hip joint bearings, Mater. Sci. Eng. C. (2017), doi:10.1016/j.msec.2017.03.211.

[44] B.S. Lee, Y. Koizumi, H. Matsumoto, A. Chiba, Collective behavior of strain-induced martensitic transformation (SIMT) in biomedical Co-Cr-Mo-N alloy polycrystal: An ex-situ electron backscattering diffraction study, Mater. Sci. Eng. A. (2014), doi:10.1016/j.msea.2014.05.071.

[45] T. Mitsunobu, Y. Koizumi, B.S. Lee, A. Chiba, Asymmetric slip trace formation in tension/compression cyclic deformation of biomedical Co-Cr-Mo-N alloy with negative stacking fault energy, Scr. Mater. (2014), doi:10.1016/j.scriptamat.2013.10.015.

[46] R. Lizárraga, F. Pan, L. Bergqvist, E. Holmström, Z. Gercsi, L. Vitos, First principles theory of the hcp-fcc phase transition in cobalt, Sci. Rep. (2017), doi:10.1038/s41598-017-03877-5.

[47] D. Wei, X. Li, W. Heng, Y. Koizumi, F. He, W.M. Choi, B.J. Lee, H.S. Kim, H. Kato, A. Chiba, Novel Co-rich high entropy alloys with superior tensile properties, Mater. Res. Lett. (2019), doi:10.1080/21663831.2018.1553803.

[48] K. Yamanaka, M. Mori, S. Sato, A. Chiba, Stacking-fault strengthening of biomedical Co-Cr-Mo alloy via multipass thermomechanical processing, Sci. Rep. (2017), doi:10.1038/s41598-017-10305-1.

[49] D. Wei, X. Li, J. Jiang, W. Heng, Y. Koizumi, W.M. Choi, B.J. Lee, H.S. Kim, H. Kato, A. Chiba, Novel Co-rich high performance twinning-induced plasticity (TWIP) and transformation-induced plasticity (TRIP) high-entropy alloys, Scr. Mater. (2019), doi:10.1016/j.scriptamat.2019.02.018.

[50] T.L. Achmad, W. Fu, H. Chen, C. Zhang, Z.G. Yang, Computational thermodynamic and first-principles calculation of stacking fault energy on ternary Co-based alloys, Comput. Mater. Sci. (2018), doi:10.1016/j.commatsci.2017.11.004.

[51] S. Lee, M.J. Duarte, M. Feuerbacher, R. Soler, C. Kirchlechner, C.H. Liebscher, S.H. Oh, G. Dehm, Dislocation plasticity in FeCoCrMnNi high-entropy alloy: quantitative insights from in situ transmission electron microscopy deformation, Mater. Res. Lett. (2020), doi:10.1080/21663831.2020.1741469.

[52] A. Taniyama, T. Takayama, M. Arai, T. Hamada, Deformation behavior of cementite in deformed high carbon steel observed by X-ray diffraction with synchrotron radiation, Metall. Mater. Trans. A Phys. Metall. Mater. Sci. (2017), doi:10.1007/s11661-017-4229-0.

[53] S. Kaboli, P.C. Burnley, In-situ synchrotron X-ray diffraction deformation and EPSC modeling of AZ31 Mg alloy, Mater. Sci. Eng. A. (2019), doi:10.1016/j.msea.2018.10.008.

[54] L. Ma, L. Wang, Z. Nie, F. Wang, Y. Xue, J. Zhou, T. Cao, Y. Wang, Y. Ren, Reversible deformation-induced martensitic transformation in Al0.6CoCrFeNi high-entropy alloy investigated by in situ synchrotron-based high-energy X-ray diffraction, Acta Mater. (2017), doi:10.1016/j.actamat.2017.02.014.

[55] P. Sedmák, P. Šittner, J. Pilch, C. Curfs, Instability of cyclic superelastic deformation of NiTi investigated by synchrotron X-ray diffraction, Acta Mater. (2015), doi:10.1016/j.actamat.2015.04.039.

[56] S. Ackermann, S. Martin, M.R. Schwarz, C. Schimpf, D. Kulawinski, C. Lathe, S. Henkel, D. Rafaja, H. Biermann, A. Weidner, Investigation of phase transformations in high-alloy austenitic TRIP steel under high pressure (up to 18 GPa) by In situ synchrotron X-ray diffraction and scanning electron microscopy, Metall. Mater. Trans. A Phys. Metall. Mater. Sci. (2016), doi:10.1007/s11661-015-3082-2.

[57] Y. Tian, S. Lin, J.Y.P. Ko, U. Lienert, A. Borgenstam, P. Hedström, Micromechanics and microstructure evolution during in situ uniaxial tensile loading of TRIP-assisted duplex stainless steels, Mater. Sci. Eng. A. 734 (2018) 281–290, doi:10.1016/j.msea.2018.07.040.

[58] D.C. Joy, D.E. Newbury, D.L. Davidson, Electron channeling patterns in the scanning electron microscope, J. Appl. Phys. (1982), doi:10.1063/1.331668.

[59] S. Zaefferer, N.N. Elhami, Theory and application of electron channelling contrast imaging under controlled diffraction conditions, Acta Mater. 75 (2014) 20–50, doi:10.1016/j.actamat.2014.04.018.

[60] S.-S. Rui, L.-S. Niu, H.-J. Shi, S. Wei, C.C. Tasan, Diffraction-based misorientation mapping: A continuum mechanics description, J. Mech. Phys. Solids. 133 (2019) 103709, doi:10.1016/j.jmps.2019.103709.

[61] M.T. Welsch, M. Henning, M. Marx, H. Vehoff, Measuring the plastic zone size by orientation gradient mapping (OGM) and electron channeling contrast imaging (ECCI), Adv. Eng. Mater. (2007), doi:10.1002/adem.200600195.

[62] S. Wei, M. Jiang, C.C. Tasan, Interstitial-free bake hardening realized by epsilon martensite reverse transformation, Metall. Mater. Trans. A Phys. Metall. Mater. Sci. 50 (2019) 3985–3991, doi:10.1007/s11661-019-05344-4.

[63] K. Nakafuji, M. Koyama, K. Tsuzaki, In-Situ electron channeling contrast imaging under tensile loading: residual stress, dislocation motion, and slip line formation, Sci. Rep. (2020), doi:10.1038/s41598-020-59429-x.

[64] H. Kriaa, A. Guitton, N. Maloufi, Fundamental and experimental aspects of diffraction for characterizing dislocations by electron channeling contrast imaging in scanning electron microscope, Sci. Rep. (2017), doi:10.1038/s41598-017-09756-3.

[65] D. Dye, H.J. Stone, R.C. Reed, A two phase elastic-plastic self-consistent model for the accumulation of microstrains in Waspaloy, Acta Mater. (2001), doi:10.1016/S1359-6454(01)00003-9.

[66] A. Wanner, D.C. Dunand, Synchrotron X-ray study of bulk lattice strains in externally loaded Cu-Mo composites, Metall. Mater. Trans. A Phys. Metall. Mater. Sci. (2000), doi:10.1007/BF02830344.

[67] M.R. Daymond, P.J. Withers, A synchrotron radiation study of transient internal strain changes during the early stages of thermal cycling in an Al/SiCw MMC, Scr. Mater. (1996), doi:10.1016/1359-6462(96)00274-6.

[68] B.H. Toby, R.B. Von Dreele, GSAS-II: The genesis of a modern open-source all purpose crystallography software package, J. Appl. Crystallogr. (2013), doi:10.1107/S0021889813003531.

[69] B. Geddes, H. Leon, X. Huang, Superalloys: Alloying and Performance, 2010.

[70] Z. Li, C.C. Tasan, K.G. Pradeep, D. Raabe, A TRIP-assisted dual-phase high-entropy alloy: Grain size and phase fraction effects on deformation behavior, Acta Mater. 131 (2017) 323–335, doi:10.1016/j.actamat.2017.03.069.

[71] R. Su, D. Neffati, S. Xue, Q. Li, Z. Fan, Y. Liu, H. Wang, Y. Kulkarni, X. Zhang, Deformation mechanisms in FCC Co dominated by high-density stacking faults, Mater. Sci. Eng. A. (2018), doi:10.1016/j.msea.2018.08.057.

[72] Y. Liu, Y. Chen, K.Y. Yu, H. Wang, J. Chen, X. Zhang, Stacking fault and partial dislocation dominated strengthening mechanisms in highly textured Cu/Co multilayers, Int. J. Plast. (2013), doi:10.1016/j.ijplas.2013.03.005.

[73] M. Naeem, H. He, F. Zhang, H. Huang, S. Harjo, T. Kawasaki, B. Wang, S. Lan, Z. Wu, F. Wang, Y. Wu, Z. Lu, Z. Zhang, C.T. Liu, X.L. Wang, Cooperative deformation in high-entropy alloys at ultralow temperatures, Sci. Adv. (2020), doi:10.1126/sciadv.aax4002.

[74] B. Clausen, T. Lorentzen, T. Leffers, Self-consistent modelling of the plastic deformation of F.C.C. polycrstals and its implications for diffraction measurements of internal stresses, Acta Mater. (1998), doi:10.1016/S1359-6454(98)00014-7.

[75] S. Cheng, A.D. Stoica, X.L. Wang, Y. Ren, J. Almer, J.A. Horton, C.T. Liu, B. Clausen, D.W. Brown, P.K. Liaw, L. Zuo, Deformation crossover: From Nano to mesoscale, Phys. Rev. Lett. (2009), doi:10.1103/PhysRevLett.103.035502.

[76] W. Woo, E.W. Huang, J.W. Yeh, H. Choo, C. Lee, S.Y. Tu, In-situ neutron diffraction studies on high-temperature deformation behavior in a CoCrFeMnNi high entropy alloy, Intermetallics (2015), doi:10.1016/j.intermet.2015.02.020.

[77] L. Balogh, G. Ribárik, T. Ungár, Stacking faults and twin boundaries in fcc crystals determined by x-ray diffraction profile analysis, J. Appl. Phys. (2006), doi:10.1063/1.2216195.

[78] R.P. Reed, R.E. Schramm, Relationship between stacking-fault energy and x-ray measurements of stacking-fault probability and microstrain, J. Appl. Phys. (1974), doi:10.1063/1.1663122.

[79] B.E. Warren, X-ray studies of deformed metals, Prog. Met. Phys. (1959), doi:10.1016/0502-8205(59)90015-2.

[80] L. Rémy, Interaction between slip and twinning systems and the influence of twinning on the mechanical behavior of FCC metals and alloys., Metall. Trans. A, Phys. Metall. Mater. Sci. (1981), doi:10.1007/BF02648536.

[81] T.H. Lee, E. Shin, C.S. Oh, H.Y. Ha, S.J. Kim, Correlation between stacking fault energy and deformation microstructure in high-interstitial-alloyed austenitic steels, Acta Mater. (2010), doi:10.1016/j.actamat.2010.01.056.

[82] M. Hillert, Phase equilibria, phase diagrams and phase transformations: Their thermodynamic basis, second edition, 2007, doi:10.1017/CBO9780511812781.

[83] C.H.P. Lupis, Chemical Thermodynamics of Materials, Prentice Hall, 1993.

[84] L.Y. Tian, R. Lizárraga, H. Larsson, E. Holmström, L. Vitos, A first principles study of the stacking fault energies for fcc Co-based binary alloys, Acta Mater (2017), doi:10.1016/j.actamat.2017.07.010.

[85] C.B. Carter, I.L.F. Ray, On the stacking-fault energies of copper alloys, Philos. Mag. (1977), doi:10.1080/14786437708235982.

[86] D.J.H. Cockayne, M.L. Jenkins, I.L.F. Ray, The measurement of stacking-fault energies of pure face-centred cubic metals, Philos. Mag. (1971), doi:10.1080/14786437108217419.

[87] Y.Y. Shang, Y. Wu, J.Y. He, X.Y. Zhu, S.F. Liu, H.L. Huang, K. An, Y. Chen, S.H. Jiang, H. Wang, X.J. Liu, Z.P. Lu, Solving the strength-ductility tradeoff in the medium-entropy NiCoCr alloy via interstitial strengthening of carbon, Intermetallics (2019), doi:10.1016/j.intermet.2018.12.009.

[88] J.B. Baudouin, G. Monnet, M. Perez, C. Domain, A. Nomoto, Effect of the applied stress and the friction stress on the dislocation dissociation in face centered cubic metals, Mater. Lett. (2013), doi:10.1016/j.matlet.2012.10.117.

[89] V. Vítek, Intrinsic stacking faults in body-centred cubic crystals, Philos. Mag. 18 (1968) 773–786, doi:10.1080/14786436808227500.

[90] G. Lu, N. Kioussis, V.V. Bulatov, Generalized-stacking-fault energy surface and dislocation properties of aluminum, Phys. Rev. B - Condens. Matter Mater. Phys. (2000), doi:10.1103/PhysRevB.62.3099.

[91] S. Ogata, J. Li, S. Yip, Energy landscape of deformation twinning in BCC and FCC metals, Phys. Rev. B - Condens. Matter Mater. Phys. (2005), doi:10.1103/PhysRevB.71.224102.

[92] M. Jo, Y.M. Koo, B.J. Lee, B. Johansson, L. Vitos, S.K. Kwon, Theory for plasticity of face-centered cubic metals, Proc. Natl. Acad. Sci. U. S. A. (2014), doi:10.1073/pnas.1400786111.

[93] K.P.D. Lagerlöf, J. Castaing, P. Pirouz, A.H. Heuer, Nucleation and growth of deformation twins: A perspective based on the double-cross-slip mechanism of deformation twinning, Philos. Mag. A. (2002), doi:10.1080/01418610208240069.

[94] L. Rémy, A. Pineau, B. Thomas, Temperature dependence of stacking fault energy in close-packed metals and alloys, Mater. Sci. Eng. (1978), doi:10.1016/0025-5416(78)90194-5.

[95] S.C. Park, L.P. Beckerman, R.E. Reed-Hill, On the portevin-le chatelier effect due to snoek strain aging in the niobium oxygen system, Metall. Trans. A, Phys. Metall. Mater. Sci. 14 A (1983) 463–469, doi:10.1007/BF02644223.

[96] Z. Lei, X. Liu, Y. Wu, H. Wang, S. Jiang, S. Wang, X. Hui, Y. Wu, B. Gault, P. Kontis, D. Raabe, L. Gu, Q. Zhang, H. Chen, H. Wang, J. Liu, K. An, Q. Zeng, T.G. Nieh, Z. Lu, Enhanced strength and ductility in a high-entropy alloy via ordered oxygen complexes, Nature 563 (2018) 546–550, doi:10.1038/s41586-018-0685-y.

[97] K. Habib, M. Koyama, T. Tsuchiyama, H. Noguchi, Dislocation motion at a fatigue crack tip in a high-nitrogen steel clarified through in situ electron channeling contrast imaging, Mater. Charact. (2019), doi:10.1016/j.matchar.2019.109930.

[98] M. Ojima, Y. Adachi, Y. Tomota, Y. Katada, Y. Kaneko, K. Kuroda, H. Saka, Weak beam TEM study on stacking fault energy of high nitrogen steels, Steel Res. Int. (2009), doi:10.2374/SRI09SP038.

[99] S. Kibey, J.B. Liu, M.J. Curtis, D.D. Johnson, H. Sehitoglu, Effect of nitrogen on generalized stacking fault energy and stacking fault widths in high nitrogen steels, Acta Mater. (2006), doi:10.1016/j.actamat.2006.02.048.

[100] Y.Z. Tian, L.J. Zhao, S. Chen, A. Shibata, Z.F. Zhang, N. Tsuji, Significant contribution of stacking faults to the strain hardening behavior of Cu-15%Al alloy with different grain sizes, Sci. Rep. (2015), doi:10.1038/srep16707.

[101] H. Wei, Y. Wei, Interaction between a screw dislocation and stacking faults in FCC metals, Mater. Sci. Eng. A. (2012), doi:10.1016/j.msea.2012.01.115.

[102] K. Rajan, Stacking fault strengthening in low stacking fault energy alloys, Scr. Metall. 17 (1983) 101–104.

[103] W.W. Jian, G.M. Cheng, W.Z. Xu, C.C. Koch, Q.D. Wang, Y.T. Zhu, S.N. Mathaudhu, Physics and model of strengthening by parallel stacking faults, Appl. Phys. Lett. (2013), doi:10.1063/1.4822323.

[104] V.S. Sarma, J. Wang, W.W. Jian, A. Kauffmann, H. Conrad, J. Freudenberger, Y.T. Zhu, Role of stacking fault energy in strengthening due to cryo-deformation of FCC metals, Mater. Sci. Eng. A. (2010), doi:10.1016/j.msea.2010.08.015.

[105] G. Zhu, L. Wang, J. Wang, J. Wang, J.-S. Park, X. Zeng, Highly deformable Mg-Al-Ca alloy with Al2Ca precipitates, Acta Mater. (2020) In press.

[106] A.H. Cottrell, LX. The formation of immobile dislocations during slip, London, Edinburgh, Dublin Philos. Mag. J. Sci. (1952), doi:10.1080/14786440608520220.

[107] A.N. Stroh, Constrictions and jogs in extended dislocations, Proc. Phys. Soc. Sect. B. (1954), doi:10.1088/0370-1301/67/5/307.

[108] P.B. Hirsch, Extended jogs in dislocations in face-centred cubic metals, Philos. Mag. (1962), doi:10.1080/14786436208201859.

[109] G. Zhu, L. Wang, H. Zhou, J. Wang, Y. Shen, P. Tu, H. Zhu, W. Liu, P. Jin, X. Zeng, Improving ductility of a Mg alloy via non-basal <a>slip induced by Ca addition, Int. J. Plast. (2019), doi:10.1016/j.ijplas.2019.04.020.

[110] M.H. Yoo, Slip, twinning, and fracture in hexagonal close-packed metals, Metall. Trans. A. (1981), doi:10.1007/BF02648537.

[111] S. Wei, J. Kim, C.C. Tasan, Boundary micro-cracking in metastable Fe 45 Mn 35 Co 10 Cr 10 high-entropy alloys, Acta Mater. 168 (2019) 76–86, doi:10.1016/j. actamat.2019.01.036.

[112] H. Wu, G. Fan, An overview of tailoring strain delocalization for strength-ductility synergy, Prog. Mater. Sci. (2020), doi:10.1016/j.pmatsci.2020.100675.